

Measuring Subsidence over Soft Clay Highways Using a Novel Time-series InSAR Deformation Model with an Emphasis on Rheological Properties and Environmental Factors (NREM)

Xuemin Xing, Yikai Zhu, Wenbin Xu, Wei Peng, and Zhihui Yuan, *Member, IEEE*

Abstract—Long-term monitoring of highways in soft soil areas, especially during the postconstruction period, is of great significance to ensure transportation safety and the quality of highway construction. Multi-temporal interferometric synthetic aperture radar (MTInSAR) provides an effective tool for soft clay highway monitoring. However, most time-series models used in MTInSAR modelling are empirical mathematical functions, which ignore the physical properties of the observed objects and may limit the accuracy of the retrieved deformation and the understanding of the underground settlement dynamics. We propose a novel InSAR time-series deformation model (namely, NREM), with emphasis on the rheological mechanisms for soft soil highways and environmental factors (temperature, humidity, and precipitation) to improve the accuracy of the traditional InSAR model and assist in the analysing the rheological properties of soft soil. The NREM is constructed based on a combination of the seasonal model and the Burgers model introduced from the field of rheology. The primary parameters (i.e., viscosity and elastic modulus) are introduced in the NREM and estimated with the generation of time-series surface deformation. In the real data experiments, two highways are selected as the test areas. The results show that the standard deviations (STDs) of the high-pass deformation, which can reflect the modelling accuracy, derived by the NREM are lower than those of the three traditional models, yielding an improvement of 45% for Lungui Highway (LH) and 50% for G1508 Highway (GH). The Root Mean Square Errors (RMSEs) for deformation results derived from NREM are estimated to be ± 5.1 mm compared with the levelling measurements, which outperform the traditional models. The obtained rheological parameters can broaden the application of InSAR technology and provide a reference for highway engineering.

Index Terms—InSAR time series, deformation monitoring, Rheology, environmental factors, soft clay, highway

I. INTRODUCTION

THE safety control of highways built on soft soil areas remains one of the primary technical matters in the field of highway subgrade engineering [1]. Due to their poor geotechnical properties, highways and roads built on soft soil areas possess more potential danger to uneven settlement and instability, which may result in serious traffic accidents under large periodical traffic loads [2], [3]. Long-term ground monitoring in the postconstruction period for soft clay highways is necessary to prevent transportation safety accidents and guarantee the quality of highway construction.

Multi-temporal interferometric synthetic aperture radar (MT-InSAR) technology, such as Permanent Scatterer Interferometry (PSI) [4] and Small Baseline Subset Interferometry (SBAS-InSAR) [5], has been confirmed to possess immense capacities for the deformation monitoring of large traffic infrastructures, such as railways, highways, and bridges [6]-[8]. This approach has complemented the deficiencies of most traditional geodetic monitoring techniques, and thus provides an effective tool for soft clay highway monitoring during the postconstruction period. The deformation modelling procedure is a crucial step for InSAR data processing. It determines the temporal-functional relationship between the deformation and unknown coefficients over the selected high coherence targets. However, the deformation models used in InSAR are commonly empirical mathematical functions composed of either one or multiple mathematical functions, which ignore the physical mechanism and deformation disciplines of the studied objects [9]-[11]. This seriously affects the precision of the final derived deformation and the subsequent deformation prediction [12]. The deformation variation with time presents a complex nonlinear

This work was supported by the National Natural Science Foundation under Grant (Nos. 42074033, 41701536, 61701047) of China; Natural Science Foundation of Hunan Province under Grant (No. 2019JJ50639); Key Project of Education Department of Hunan Province under Grant (No.18A148). (*Corresponding author: Wenbin Xu*)

X. Xing, Y. Zhu, and W. Peng are with the School of Traffic and Transportation Engineering, Changsha University of Science & Technology, Changsha 410014, China, and also with the Laboratory of Radar Remote Sensing Applications, Changsha University of Science & Technology, Changsha 410014, China (e-mail: xuemin.xing@csust.edu.cn; zhuikai@whu.edu.cn; pengwei@csust.edu.cn).

W. Xu is with the School of Geosciences & Info-physics, Central South University, Changsha 410083, China (e-mail: wenbin.xu@csu.edu.cn).

Z. Yuan is with the School of Electrical & Information Engineering, Changsha University of Science & Technology, Changsha 410014, China, and also with the Laboratory of Radar Remote Sensing Applications, Changsha University of Science & Technology, Changsha 410014, China (e-mail: yuanzhihui@csust.edu.cn).

characteristic for soft clay highways. It cannot truly reflect the deformation law by using a single empirical function to fit the physical variations of highways, which will inevitably influence the precision and reliability of the observed deformation as well as the following stage of deformation interpretation [13]. Based on the deficiencies of traditional models, scholars have attempted to introduce physical parameters into the process of InSAR modelling, and have successfully improved the accuracy of the obtained subsidence. For instance, Zhao et al. (2016) replaced the conventional model of linear velocity by combining the polynomial model and external environmental factors (temperature and precipitation), which improved the deformation accuracy over permafrost and assisted the subsequent interpretation [14]. Wang et al. (2016) adopted a combined simplified Stefan equation and a periodical function to model the seasonal variations over permafrost [15]. Yang et al. (2018) presented an advanced method by combining InSAR with a temporal probability integral method that has proven to be effective and reliable in the large-scale subsidence monitoring of coal mines [16].

In the field of geotechnical mechanics, numerous studies have shown that the displacement of soft soil is significantly affected by the rheology of soil [17], [18]. The rheological property is a primary engineering characteristic of soft soil, which defines the phenomenon where deformation is related to time; namely, the time effect [19]. Rheological parameters (i.e., the elastic modulus and viscosity) are important indexes for characterizing the rheological properties of soft soil [20]. Any soil is impacted by rheological properties; thus, if the rheological properties of soft clay can be integrated into InSAR temporal deformation modelling and the rheological property coefficients can be introduced into traditional models, then the accuracy of long-term deformation monitoring after highway construction will be considerably improved. Moreover, the physical parameters and significance of the model can assist in interpreting the subsequent deformation results and provide a reference for the field of geotechnical mechanics. Accordingly, Xing et al. (2019) proposed an improved model for a deformation time-series considering the rheological parameters, i.e., the elastic modulus and viscosity, based on the Kelvin rheological model (KM), which was successfully applied to the subsidence monitoring of soft clay highways [21]. The KM is constructed under the critical state of the physical parameters and transferred from the Burgers model (BM), describing the rheological properties of the solid. In fact, the soil contained in soft clay is a three-phase body simultaneously composed of solid, liquid, and gas, which cannot be completely described by a pure KM [22]. Additionally, the KM only considers the internal factors of soft clay, ignoring the influence of external environmental factors on the deformation variations. In 2018, we conducted an in-depth study on the periodic variation in deformations over highways in soft clay areas and detected an apparent periodic variation law in the surface deformation of the two highways from October 2014 to November 2015. Seasonal fluctuations were suggested as being related to the local precipitation and temperature [23].

In this study, we propose a novel deformation model (namely NREM), which takes an integrated consideration of the physical parameters of rheology, external environmental factors

(temperature, precipitation, and humidity), and seasonal variation characteristics into traditional SBAS-InSAR technology. In this work, the four-element rheological model, i.e., the BM, is selected to model the rheological component describing the temporal correlation between the line-of-sight (LOS) deformation of radar and the unknown rheological coefficients. The BM is constructed through a connection series of Maxwell and Kelvin bodies. As a common viscoelastic model, it can generate instantaneous elastic deformation at the beginning of loading, and is accompanied by viscous and plastic deformation at the end. During the unloading stage, the BM can reveal elastic recovery and residual permanent deformation [24]. Consequently, the BM is adopted to reflect the rheological properties of the soft clay area.

This work first introduced the methodology for constructing the NREM and the parameter estimation algorithm. Then, both a simulated experiment and a real data experiment were designed to verify the NREM. In the real experiment, the rheological parameters of the soft clay layer in certain segments of the Lungui Highway (LH) and G1508 Highway (GH) in Guangdong Province, China, were obtained, and the time-series deformation results from January 2015 to January 2017 were inverted. Subsequently, residual high-pass (HP) deformation and levelling measurements were adopted to estimate the accuracy of the NREM. The potential causes of the deformation, including environmental factors and rheological properties, were discussed in detail, and a correlation analysis and a sensitivity analysis were executed in the discussions. Finally, conclusions with a brief prospect for the future plan was introduced.

II. METHODOLOGY

A. Construction of the NREM

1) *Accounting for the rheological properties:* Here the BM is selected to establish the NREM, which is a commonly used one-dimensional model in the field of rheology. The rheological model is composed of various rheological elements, such as elastic elements (spring), viscous elements (glue spot), and plastic elements (slider) with different connection modes. For example, the KM is a parallel-connected system with a glue spot and a spring, while the Maxwell model (MM) is a series-connected system with the same elements. The BM is a series structure with the KM and MM. Fig. 1 is a schematic drawing of the integrated components of the BM. The rheological constitutive equation of the BM can be expressed as [25]:

$$\varepsilon = \frac{\sigma_c}{E_2} + \frac{\sigma_c}{\eta_2} t + \frac{\sigma_c}{E_1} (1 - e^{-\frac{E_1 t}{\eta_1}}) \quad (1)$$

where ε represents the strain and σ_c defines the external loading, which is treated as constant. The external load for the highway during the postconstruction period is mainly induced by the gravity of the road layer and the load of vehicles. In the actual deformation analysis, the vehicle load is negligible compared to the road layer's gravity. The gravity of the road layer is usually acquired via in situ investigation of the highway structure and the gravity test of soil in the upper soft clay layer. E_1 and E_2 represent the elastic modulus of the material, and

η_1 and η_2 define the viscosity. E_1 , E_2 , η_1 and η_2 are significant rheological parameters in rheology theory, which are treated as unknown parameters here, and t defines the total time span during the period of strain occurrence.

The vertical subsidence of soft soil d_1 can be written as the temporal function of ε [26]:

$$d_1 = \int_{t_1}^{t_2} \int_0^H \varepsilon \cdot dh dt \quad (2)$$

where t_1 and t_2 define the starting and stopping moments of the deformation, respectively, H defines the mean thickness of the soft soil layer, and h and t represent the thickness of the soft clay layer and the time span of the deformation, respectively. Combining (1) and (2), d_1 can be further written as:

$$\begin{aligned} d_1 = & \frac{H\sigma_c}{E_2^2}(t_2 - t_1) + \frac{H\sigma_c}{2\eta_2}(t_2^2 - t_1^2) \\ & + \frac{H\sigma_c}{E_1}(t_2 - t_1) + \frac{H\sigma_c\eta_1}{E_1^2}(e^{-\frac{E_1}{\eta_1}t_1} - e^{-\frac{E_1}{\eta_1}t_2}) \end{aligned} \quad (3)$$

where the rheological parameters E_1 , E_2 , η_1 and η_2 are regarded as the unknown parameters.

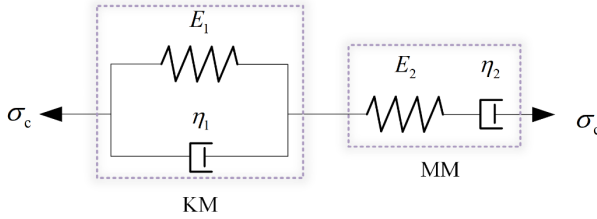


Fig. 1. Burgers rheological model (σ_c is the external constant loading; E_1 and E_2 define the elastic modulus, respectively; η_1 and η_2 define the viscosity).

2) *Accounting for the seasonal variation:* As discussed above, the seasonal variation in the temporal characteristics of the soft soil cannot be ignored. The low-pass (LP) component of the surface deformation related to the seasonal variation can be written as the combination of a linear component and a periodical component, which can be expressed as [27]:

$$\begin{aligned} d_2 = & v_1(t_2 - t_1) + v_2[\sin(\frac{2\pi}{T}t_2) - \sin(\frac{2\pi}{T}t_1)] \\ & + v_3[\cos(\frac{2\pi}{T}t_2) - \cos(\frac{2\pi}{T}t_1)] \end{aligned} \quad (4)$$

where T represents a one-year period of 365 days, and v_1 , v_2 and v_3 are treated as unknown parameters here.

3) *Accounting for the external environmental factors:* According to [28] and [29], surface deformation is suggested to be highly related to the variations in the groundwater level, which is affected by underground water exploitation and external environmental factors (i.e., temperature, precipitation, and humidity). Hence, the effect of external climate factors will

be considered in the time-series deformation model here. On this basis, we put forward the following deformation model:

$$d_3 = \sum_{n=1}^k \alpha_n A_n(t) \quad (5)$$

where d_3 defines the ground deformation related to the external climate factors; k denotes the quantity of the environmental indexes; A_n represents the n^{th} external factors; and α_n represents the coefficient of the n^{th} environmental factors.

Three external environmental factors, including temperature, humidity, and precipitation, are considered here. Therefore, (5) can be written as:

$$\begin{aligned} d_3 = & \alpha_1[T(t_2) - T(t_1)] + \alpha_2[H(t_2) - H(t_1)] \\ & + \alpha_3[P(t_2) - P(t_1)] \end{aligned} \quad (6)$$

where $T(t)$ is the monthly average temperature at date t , $H(t)$ represents the monthly average humidity, $P(t)$ denotes the monthly total precipitation, and α_1 , α_2 and α_3 are treated as the unknown parameters.

4) *The integrated NREM:* Based on the integration of the aforementioned three components, the NREM can be constructed. The LP deformation is regarded as a summary of the rheological component d_1 , the seasonal component d_2 , and the external environmental component d_3 . Combining (3), (4), and (6), the final deformation model can be expressed as:

$$\begin{aligned} d = & d_1 + d_2 + d_3 \\ = & \frac{H\sigma_c}{E_2^2}(t_2 - t_1) + \frac{H\sigma_c}{2\eta_2}(t_2^2 - t_1^2) + \frac{H\sigma_c}{E_1}(t_2 - t_1) \\ & + \frac{H\sigma_c\eta_1}{E_1^2}(e^{-\frac{E_1}{\eta_1}t_1} - e^{-\frac{E_1}{\eta_1}t_2}) + \alpha_1(T(t_2) - T(t_1)) \\ & + \alpha_2(H(t_2) - H(t_1)) + \alpha_3(P(t_2) - P(t_1)) \\ & + v_1(t_2 - t_1) + v_2(\sin(\frac{2\pi}{T}t_2) - \sin(\frac{2\pi}{T}t_1)) \\ & + v_3(\cos(\frac{2\pi}{T}t_2) - \cos(\frac{2\pi}{T}t_1)) \end{aligned} \quad (7)$$

For each interferogram, t_1 and t_2 represent the acquisition dates of the master and slave images, respectively. The rheological deformation of the soft soil mainly consists of shearing deformation and vertical compression. Since vertical compression is taken as the major deformation effect for a highway engineering analysis and the external stress induced by the upper gravity of the highway σ_c is considered to be the only constant external load in (1), we only consider the effect of vertical deformation here [26]. When ignoring horizontal movement, the vertical subsidence can be calculated as $d = d_{\text{LOS}}/\cos\theta$ [30]. The phase at each point of the wrapped interferogram can be written as:

$$\begin{aligned}
 \varphi_j(x, r) = & \frac{4\pi \cos \theta}{\lambda} \left[\frac{H\sigma_c \eta_1(x, r)}{E_1^2(x, r)} \left(e^{-\frac{E_1(x, r)}{\eta_1(x, r)} t_1} - e^{-\frac{E_1(x, r)}{\eta_1(x, r)} t_2} \right) \right. \\
 & + \frac{H\sigma_c}{E_2^2(x, r)} (t_2 - t_1) + \frac{H\sigma_c}{2\eta_2(x, r)} (t_2^2 - t_1^2) \\
 & + \frac{H\sigma_c}{E_1(x, r)} (t_2 - t_1) + \alpha_1(x, r) (T(t_2) - T(t_1)) \\
 & + \alpha_2(x, r) (H(t_2) - H(t_1)) \\
 & + \alpha_3(x, r) (P(t_2) - P(t_1)) + v_1(x, r) (t_2 - t_1) \\
 & + v_2(x, r) (\sin(\frac{2\pi}{T} t_2) - \sin(\frac{2\pi}{T} t_1)) \\
 & + v_3(x, r) (\cos(\frac{2\pi}{T} t_2) - \cos(\frac{2\pi}{T} t_1)) \\
 & \left. + \frac{4\pi B_\perp \Delta z(x, r)}{\lambda r_j \sin \theta_j} + \Delta \varphi_{j, \text{res}}(x, r) \right] \quad (8)
 \end{aligned}$$

where j defines the index of the interferogram, (x, r) represents the SAR coordinates of the target, λ represents the radar wavelength, B_\perp defines the spatial baseline, Δz defines the height corrections, r_j is the sensor-target range, and $\Delta \varphi_{j, \text{res}}(x, r)$ represents the residual phase. Supposing there are M interferometric pairs generated, M phase equations can be established. The $P = (E_1, E_2, \eta_1, \eta_2, \alpha_1, \alpha_2, \alpha_3, v_1, v_2, v_3, \Delta z)$ are regarded as unknown parameters. Suppose at least 11 observations are acquired, and the unknown parameters, including the rheological parameters of all the high coherence points, can be solved.

B. Parameter estimation

After the process of InSAR modelling as introduced above, the unknown parameter P should be estimated accurately and reliably, which will be used as the input data for the generation of LP deformation (described as equation (7)). The parameter estimation for equation (8) is a nonlinear estimation problem, which can be solved by the Genetic Algorithm (GA). GA possesses the advantages of global optimization and not affected by individual parameters and specific forms of models. However, the disadvantages of slow convergence speed and low accuracy are also prominent for GA. Consequently, the combination of GA and the Simplex Algorithm (SA), namely GA-SA, is adopted here to effectively estimate the unknown parameters [31]. The individual genes of the population for GA-SA can be written as $P = (E_1, E_2, \eta_1, \eta_2, \alpha_1, \alpha_2, \alpha_3, v_1, v_2, v_3, \Delta z)$ in (8). The specific searching process for GA-SA is as follows:

1) GA-SA obtains the optimized population individual according to the minimum norm principle. Thus, firstly, the fitness function should be constructed according to the minimum norm principle of the model residual phase, which can be written as:

$$f = \|\Delta \varphi_{j, \text{res}}(x, r)\| = \min \quad (9)$$

2) The indexes of the population size, iteration times, and individual population genes are preliminarily set. Then, the estimated value of f based on the initial population individuals can be calculated.

3) And then the selection, crossover, and mutation operations of each population are executed, and the final optimized individuals are generated [32], [33]. Whether it meets the iterative termination conditions should then be determined. If not satisfied, the cross-mutation operation will be executed, generating the next population. If satisfied, the best population of the individuals will be output, which will be determined as the final GA-generated optimal parameter. Accordingly, the algorithm will be ended.

4) Finally, the SA is utilized to refine the solutions obtained by GA, which is introduced into our experiment. The GA-derived solutions are regarded as the initial input values of SA, and the optimized output solutions are considered as the final estimated parameters.

C. Surface deformation estimation based on NREM

After the unknown parameters at each pixel (x, r) of the NREM are obtained, the LP deformation during the SAR acquisition dates can be acquired through (7). Similarly, the LP deformation can be calculated on a point-by-point basis. Temporal HP filtering and spatial LP filtering were executed for the residual phase mentioned in (8) in order to extract the HP component [14]. The final total deformation can be generated by the summation of the HP and LP components. The flow chart of the time-series deformation generation based on NREM is shown in Fig. 2.

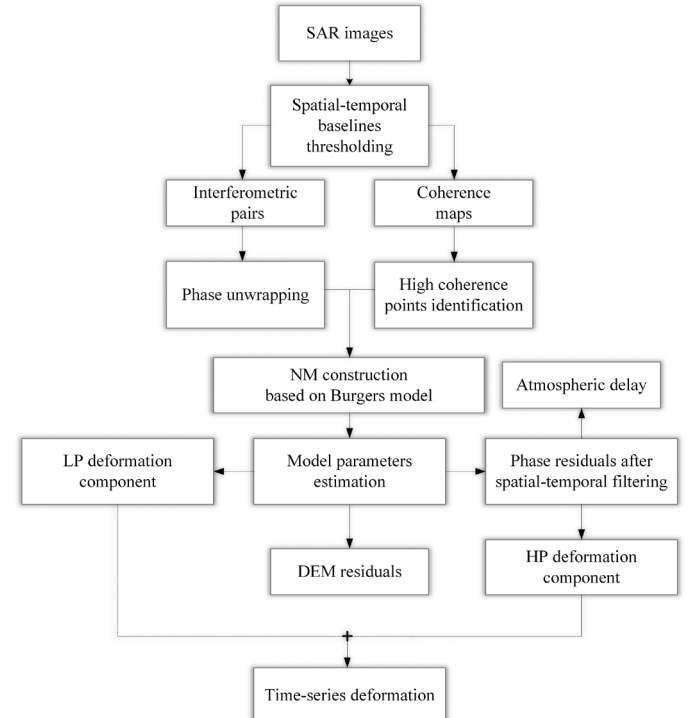


Fig. 2. Flow chart of the time-series deformation generation based on the NREM.

III. SIMULATED EXPERIMENT

The initial intervals for the magnitudes of the rheological parameters were set as follows: $E_1 \in [0, 30]$ MPa; $E_2 \in [0, 50]$ MPa; $\eta_1 \in [0, 10] \times 10^6$ MPa.s; $\eta_2 \in [0, 20] \times 10^6$ MPa.s, which were determined considering both the specific one-dimensional consolidation rheological tests and the ranges introduced in [34] and [35]. According to the existing experimental results [23], the linear rates v_1 in this embodiment were set within [-0.2, 0.1] m/yr, and the seasonal rates v_2 and v_3 were controlled within [-0.1, 0.05] m/yr. The coefficients of the environmental factors were set by consulting the reference [14], which were as follows: $\alpha_1 \in [-3, 0]$ mm/°C; $\alpha_2 \in [0, 2]$ mm/%; and $\alpha_3 \in [0, 0.1]$ mm/mm. Two hundred high coherence pixels were then generated in total. The field of rheological parameters E_1 , E_2 , η_1 and η_2 was generated using the two-dimensional Gaussian function. The height corrections Δz was simulated using a Gaussian random simulator. The utilized SAR sensor parameters were set following the TerraSAR-X imaginary (Stripmap descending). According to the SBAS-InSAR-generated processing interferograms in the real experiment, the parameters of interferometric pairs with a good quality were selected as the known SAR sensor parameters. The values of 200 high coherence points can be extracted from the simulated field of each parameter as the real values, which could be used to verify the accuracy of the generated estimations through GA-SA.

In order to evaluate the impacts of different temporal baseline connection modes and different numbers of interferometric pairs on the corresponding estimated parameters, two groups of simulation with ten original images (under single-master connection and multi-master connection, respectively) were designed firstly. For each group, six subgroups of simulation were carried out. The number of interferometric pairs for each subgroup was 10, 15, 20, 25, 30, and 35, respectively, which also represented the number of InSAR phase functions for (8). For each subgroup, the corresponding GA-SA procedure was

performed to obtain the unknown NREM parameters based on the simulated InSAR phase observations, and the final estimated subsidence could be obtained via equation (7). Fig. 3 reveals the quantitative comparison of relative errors of each model parameters under different numbers of pairs and network connection. Obviously, the relative errors of rheological parameters E_1 , E_2 , η_1 , and η_2 are more susceptible to the number of interferometric pairs, among which E_2 is the most vulnerable parameter. For both groups, generally, the relative errors for both the two groups decrease with the increase of interferometric numbers. As the number of interferograms varies from 10 to 35, the relative errors of E_2 dwindled from 7.8% to 4.2%, with an improvement of 46% under the single-master connection. Conversely, Δz appears as the most stable one when the number of interferograms increases. Consequently, a relatively total number higher than 30 and a multi-master connection mode are recommended in the real data experiment when adopting our approach.

As we have outlined above, in order to demonstrate the feasibility of GA-SA more intuitively and quantitatively, a comparison between the estimated parameters via GA-SA and the simulated real values under a multi-master connection with 30 interferometric pairs is displayed in Fig. 4. As it shows, under a 0.5 mm noise variance, the blue circles are highly consistent with the red pentagons, indicating that the estimated values obtained by the simulated experiment are highly consistent with the real values. The Root Mean Square Errors (RMSEs) for each parameter and its corresponding relative error proportion are listed in Table I. As it shows, with the increase of noise level (from 0.5 mm to 2.5 mm noise variances), the RMSEs of each parameter increases gradually, with the maximum relative error accumulated to 4.5% for η_2 and 4.3% for η_1 , respectively. The RMSEs of all the unknown parameters occupies lower than 5% of the estimated maximum magnitudes, indicating a permitted error range for algorithm.

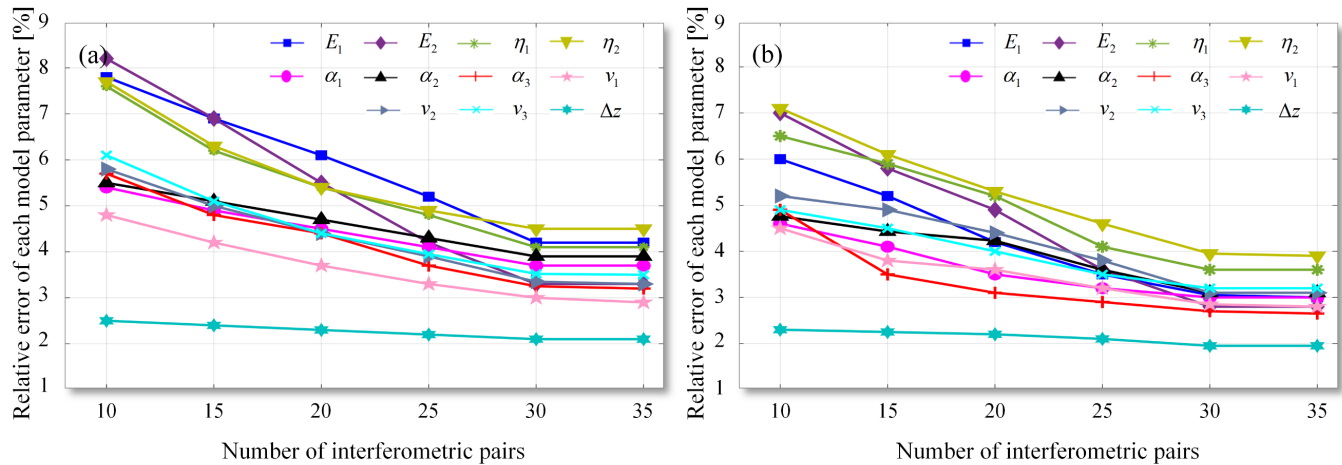


Fig. 3. The relative errors of each model parameter under different numbers of interferometric pairs: (a) single-master connection; (b) multi-master connection.

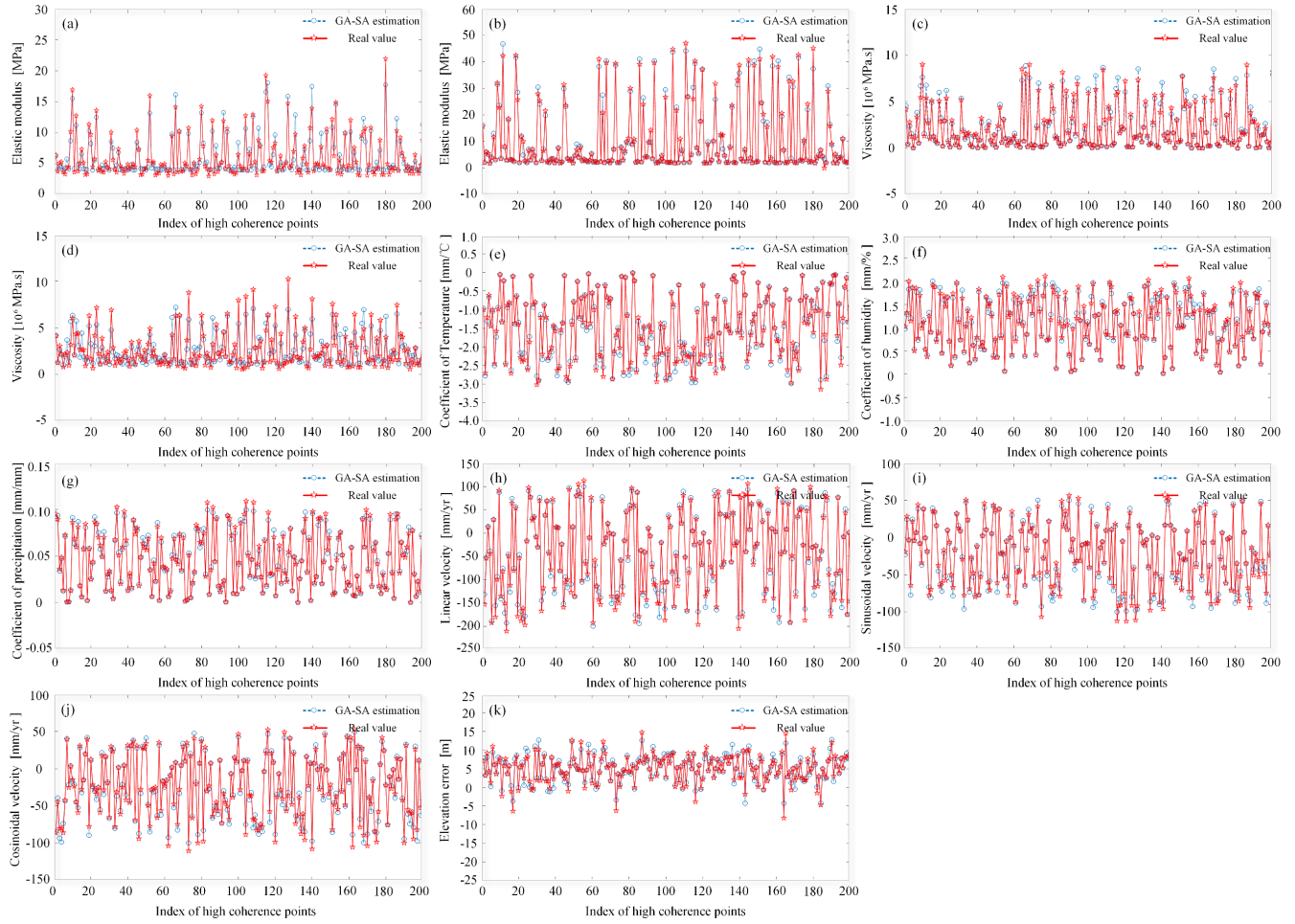


Fig. 4. GA-generated values compared with real values in the simulation (under a 0.5 mm noise variance): (a) E_1 ; (b) E_2 ; (c) η_1 ; (d) η_2 ; (e) α_1 ; (f) α_2 ; (g) α_3 ; (h) v_1 ; (i) v_2 ; (j) v_3 ; (k) Δz

TABLE I
RMSEs of each parameter in the simulation with different noise levels

Unknown parameters	Noise level				
	0.5mm	1.0 mm	1.5 mm	2.0 mm	2.5 mm
E_1 (MPa)	± 0.88 (3.0%)	± 0.92 (3.1%)	± 0.95 (3.2%)	± 1.01 (3.4%)	± 1.04 (3.5%)
E_2 (MPa)	± 1.38 (2.8%)	± 1.43 (2.9%)	± 1.48 (3.0%)	± 1.50 (3.1%)	± 1.53 (3.1%)
η_1 (10^6 MPas)	± 0.36 (3.6%)	± 0.38 (3.8%)	± 0.41 (4.1%)	± 0.42 (4.2%)	± 0.43 (4.3%)
η_2 (10^6 MPas)	± 0.78 (3.9%)	± 0.81 (4.1%)	± 0.85 (4.3%)	± 0.87 (4.4%)	± 0.89 (4.5%)
α_1 (mm°C)	± 0.09 (3.0%)	± 0.09 (3.1%)	± 0.09 (3.1%)	± 0.09 (3.2%)	± 0.10 (3.2%)
α_2 ($\text{mm}/\%$)	± 0.06 (3.1%)	± 0.06 (3.2%)	± 0.07 (3.3%)	± 0.07 (3.4%)	± 0.07 (3.5%)
α_3 (mm/mm)	± 0.0027 (2.7%)	± 0.0028 (2.8%)	± 0.0030 (3.0%)	± 0.0030 (3.1%)	± 0.0031 (3.1%)
v_1 (mm/yr)	± 8.3 (2.8%)	± 8.6 (2.9%)	± 9.0 (3.0%)	± 9.3 (3.1%)	± 9.8 (3.3%)
v_2 (mm/yr)	± 4.7 (3.1%)	± 5.2 (3.4%)	± 5.5 (3.6%)	± 5.8 (3.8%)	± 6.1 (4.0%)
v_3 (mm/yr)	± 4.8 (3.2%)	± 5.1 (3.4%)	± 5.4 (3.7%)	± 5.8 (3.8%)	± 5.8 (3.9%)
Δz (m)	± 0.97 (1.9%)	± 0.99 (2.0%)	± 0.99 (2.0%)	± 1.02 (2.1%)	± 1.05 (2.1%)

IV. REAL DATA EXPERIMENTS

A. Background of the study area

Two typical soft clay highways, Lungui Highway (LH) and G1508 Highway (GH) in Foshan, China, are chosen as the test areas (as represented in Fig. 5), which belong to the Pearl River Delta. The Pearl River Delta is one of the four major deltas in China, covering an area of 8601.1 square kilometres, ranking 15th among all deltas worldwide. The Pearl River Delta is formed by three regressions and three transgressions. The soft soil deposited by marine facies in the Pearl River Delta is mainly distributed in the middle of the delta. Foshan, near the middle of the delta, is a continuous deposit of silt. The natural water content of the soil ranges from 70% to 85% and the void ratio is within the interval of 1.5 to 1.8. The microstructure of the soft clay in the Shunde District is primary cavernous aggregates consisting of clay particles. The pores are evenly distributed among aggregates with a high clay content (higher than 30%), a loose structure, and a low strength [36].

Both LH and GH are significant transportation hubs and connect multiple highways and roads in the city. Soft clay is the main soil along both routes. LH is also one of the three major south-north transportation lines in Foshan, with soft soil being the primary subgrade component along the route. GH, located

in the southern part of the Shunde District, was opened to traffic in 2010. As recorded in the design standards, the permissible vertical subsidence during the postconstruction period is 30 cm/yr for regular highways. As the Foshan Transportation Bureau introduced, the traffic passenger flow volume was up to 2295.21 million people per kilometre, which indicates the vital traffic situation for both highways. Muddy clay and silt with a soft-plastic behaviour dominate the geotechnical components of the two highways. As shown in Fig. 5(b), we can see that both the two highways are surrounded by a slew of waterways (such as the Shunde Tributary Waterway, the Donghai Waterway, the Ronggui Waterway, the Shunde Waterway, the Tanzhou Waterway, and the Guizhou Waterway), which have great impact in promoting the underground development of soft soil. In accordance with the hydrogeological conditions of the Shunde District, precipitation and temperature are the primary environmental factors.

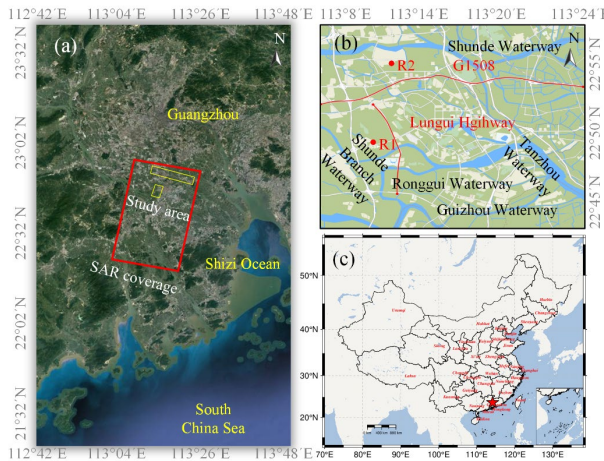


Fig. 5. Study area: (a) The TerraSAR-X image coverage. The red rectangle represents the spatial coverage of the SAR images, and the yellow rectangles represent the study areas in this work. (b) Enlarged map of the two highways using Google Maps as the background. The red curves define the two highways. The reference points for LH and GH are shown as R1 and R2, respectively. (c) A map of the location in China.

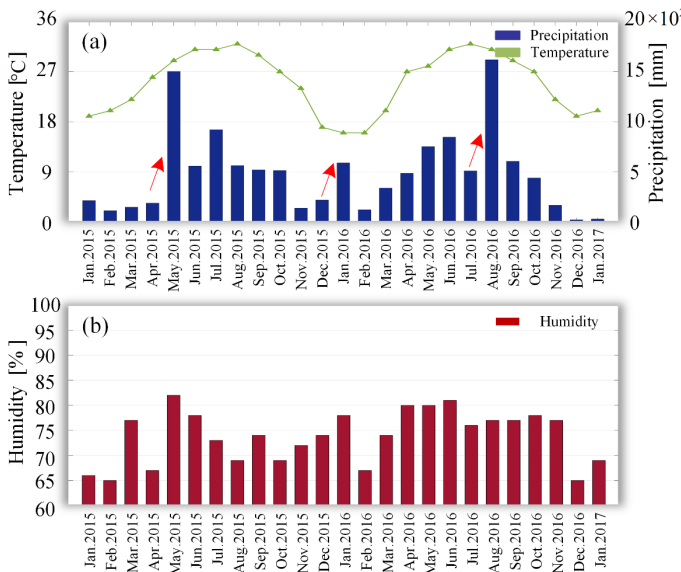


Fig. 6. Collected external environmental data: (a) monthly mean air temperature and total precipitation from January 2015 to January 2017; and (b) monthly average humidity from January 2015 to January 2017.

B. SAR acquisition and data processing

In total, 23 TerraSAR-X images (Stripmap descending mode) were collected. The main period was from January 1, 2015, to January 18, 2017. As shown in Fig. 5(a), the study area is marked with a yellow solid rectangle, and the two test highways are marked by the red solid rectangle, with a spatial coverage of approximately 1817 km². Fig. 6 shows the data of the external environmental factors over this area, including the average monthly air temperature, humidity, and precipitation. Thresholds of 250 m and 365 days were set empirically for the temporal-spatial baseline in the pre-processing of unwrapped interferograms. A total of 108 interferograms for both highways were obtained. An improved Goldstein filter was utilized to suppress the noise further [37]. The reference points R1 (LH area) and R2 (GH area) of phase unwrapping are located on the roofs of the residential area near Nanguo West Road and Xinglei Middle Road, respectively, which were treated as stable. The reference points were determined after a meticulous in-situ investigation precisely and empirically at the study area. The roofs of the building were far away from the waterways and silt area (which was treated as the most unstable soil), and both the two buildings were built on foundations after a reinforcement treatment.

As indicated from the simulated experiment introduced in III, the relative errors of the estimated unknown parameter tend to be stable as the number of interferometric pairs equal to or higher than 30. According to this principle, and considering the computational efficiency for the following GA searching, the procedure of interferometric combination was carried out. Firstly, the two test areas were cut out respectively from the SAR images and the following procedures including the interferometry and phase unwrapping were conducted separately. With two different unwrapping reference points R1 and R2 (shown in Fig. 5(b)) located at different areas, the coherence and unwrapping results of the two test areas were slightly different. Accordingly, the numbers were different for the two test areas. Then, the spatio-temporal baselines were set strictly (with the thresholds of 130 m and 365 days respectively), which generated a total of 108 interferometric pairs for both two groups. Then, according to the generated coherence maps and the unwrapped interferograms, the interferograms with poor coherence and abnormal unwrapping results, especially nearby the two highways, were eliminated artificially. Meanwhile, we also ensured that no isolated image existed after the combination. For LH, 48 images of low coherence and 53 images of poor unwrapping fringes were eliminated, while for GH, 28 images of low coherence and 62 images of poor unwrapping fringes were removed from the combination. Finally, a total number of 32 for LH and 35 for GH interferometric pairs were obtained, and those pairs are high-quality ones. The temporal and perpendicular baselines of the final selected interferograms are shown in Fig. 7.

During the process of high coherence points identification, we manually masked off those high coherence points located outside the highways. The reasons are as follows: firstly, in the highway area, the grace of the subgrade and traffic load will provide corresponding vertical pressure to the soft soil, which is necessary for the rheological mechanism. In contrast, areas beyond the highways are without the pressure of rheological

condition. Secondly, some residential areas near the highways may not consist of pure soft soil (some buildings were built on foundations after reinforcement treatment). Therefore, we masked out the areas along the highways in our work, and focused on the spatio-temporal characteristics highly related to the rheological mechanism. The high coherence targets were identified based on three indexes, including the amplitude deviation, the average coherence, and the intensity automatically after 45 groups of identification experiments. A total of 875 and 1124 candidates were extracted for LH and GH, respectively [38].

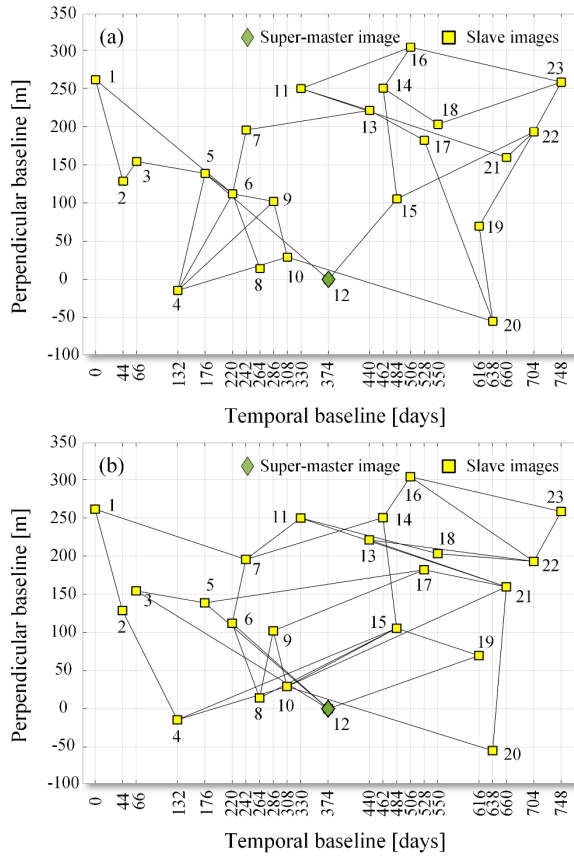


Fig. 7. Perpendicular and temporal baselines of selected interferometric pairs (x axis defines the accumulated days with reference to the acquisition date of the first SAR image, y axis represents the perpendicular baseline and the green rhombus stands for the super-master image): (a) LH; (b) GH.

The initial individual genes were set preliminarily as follows: $E_1 \in [0, 30]$ MPa, $E_2 \in [0, 50]$ MPa, $\eta_1 \in [0, 10] \times 10^6$ MPa.s, $\eta_2 \in [0, 20] \times 10^6$ MPa.s, $\alpha_1 \in [-3, 0]$ mm/ $^\circ$ C, $\alpha_2 \in [0, 2]$ mm%, $\alpha_3 \in [0, 0.1]$ mm/mm, $v_1 \in [-0.2, 0.1]$ m/yr, $v_2 \in [-0.1, 0.05]$ m/yr, $v_3 \in [-0.1, 0.05]$ m/yr, and $\Delta z \in [-15, 15]$ m. Through the field investigation and indoor one-dimensional consolidation rheological tests, the external load σ_c was set as 0.25 MPa. In the process of GA searching, the upper limit of the population was determined as 1000 generations and 1000 individuals for each generation. A two-point crossover was adopted, and the probability was set as 0.7. The minimum value of the average fitness was regarded as the iteration termination condition. With the obtained parameters generated by GA and SA, the LP surface deformation can be estimated according to (6). The HP deformation component was recovered from the

residual phase component via temporal-spatial HP-LP filtering [14]. Finally, the deformation time-series of all the high coherence points were acquired through summation.

C. Experimental results and validation

1) Estimated model parameters of NREM: The estimated parameters for the NREM over each selected high coherence point in (8) are presented in Fig. 8 (LH) and Fig. 9 (GH). For the LH, we can see from Fig. 8(a)-(d) that the elastic moduli E_1 and E_2 are generally distributed within the range of [10, 25] MPa and [5, 20] MPa, respectively, whereas the viscosity and η_2 are distributed in $[0, 10] \times 10^6$ MPa.s and $[0, 7] \times 10^6$ MPa.s, respectively. Similar ranges of E_1 , η_1 and η_2 for GH are shown in Fig. 9(a), (b), and (d). Comparatively, the elastic modulus E_2 is distributed within [5, 15] MPa, with the colour ranging from red to yellow. As observed, the four rheological parameters of the LH and GH exhibit a similar distribution pattern: a relatively lower value in the riverside and a higher value in the inland area. According to the hydrogeological conditions, GH is in a suburban area surrounded by many fish ponds, lakes, and rivers. The underground water supply of the soft clay in the study area is adequate, leading to more distinct rheological properties. For instance, the obtained rheological parameters (E_1 , E_2 , η_1 , and η_2) of point A (located in the riverside area) were 6.97 MPa, 7.92 MPa, 4.22×10^6 MPa.s, and 4.55×10^6 MPa.s, respectively, whereas for point C in the inland area, the values were 23.01 MPa, 18.02 MPa, 9.73×10^6 MPa.s, and 6.32×10^6 MPa.s, respectively. The main types of soft clay distributed in Foshan City are alluvial silt and muddy soil, which exist in the form of a thick layer and interlayer. The indoor tests for the soil properties in this area based on numerous studies show that the soil along the waterways was primarily mucky clay, E_1 was distributed mainly within [0, 10] MPa, E_2 within [2, 8] MPa, η_1 ranged from 0 to 5×10^6 MPa.s, η_2 was in the interval of $[1, 5] \times 10^6$ MPa.s, and the soil of the inland area was primarily composed of mucky clay and mealy sand. E_1 was mainly distributed at [15, 25] MPa, E_2 within [5, 20] MPa, η_1 ranged from 4×10^6 to 10×10^6 MPa.s, and η_2 was within the interval [4, 7] $\times 10^6$ MPa.s [34], [35]. The indoor test results were consistent with the magnitude obtained in our work. Additionally, we found an interesting phenomenon in which the lower the rheological parameter value is, the higher the deformation is. Consequently, the values of rheological parameters acquired from our experiment can reflect the deformation characteristics of the study area spatially. The linear velocity, periodic coefficients, coefficients of the environmental factors, and height corrections are shown in Fig. 8(e)-(k) and Fig. 9(e)-(k), respectively, for both test highways.

2) Ground deformation characteristics: After the model parameters of the NREM are determined for each target, the time-series deformation between the dates of SAR acquisitions can be calculated according to (7). The results are presented in Fig. 10 and Fig. 11, respectively. We can see the spatial distribution for LH in Fig. 10. As shown, there are three major subsidence regions concentrated in the riverside area (marked as purple rectangles L1 and L2) with a maximum settlement of 123 mm. However, the deformation is significantly weaker in

the inland area (generally yellow), with a maximum subsidence of 65 mm. Temporally, we determined that the overall accumulated deformation was characterized by a completely subsiding trend with periodical variations. As shown in Fig. 10, subsidence began on January 01, 2015, and a slight uplift occurred from March 08 to May 13, 2015. Then, a subsequent

subsiding lasted until December 27, 2016. A decreasing trend occurred again from November 27, 2015, to January 10, 2016, with a recovery of up to 12 mm. Another jump appeared from July 04, 2016, to September 08 2016, with a recovery of nearly 40 mm. The peak accumulated subsidence for LH occurred on January 18, 2017, with a magnitude of -123 mm.

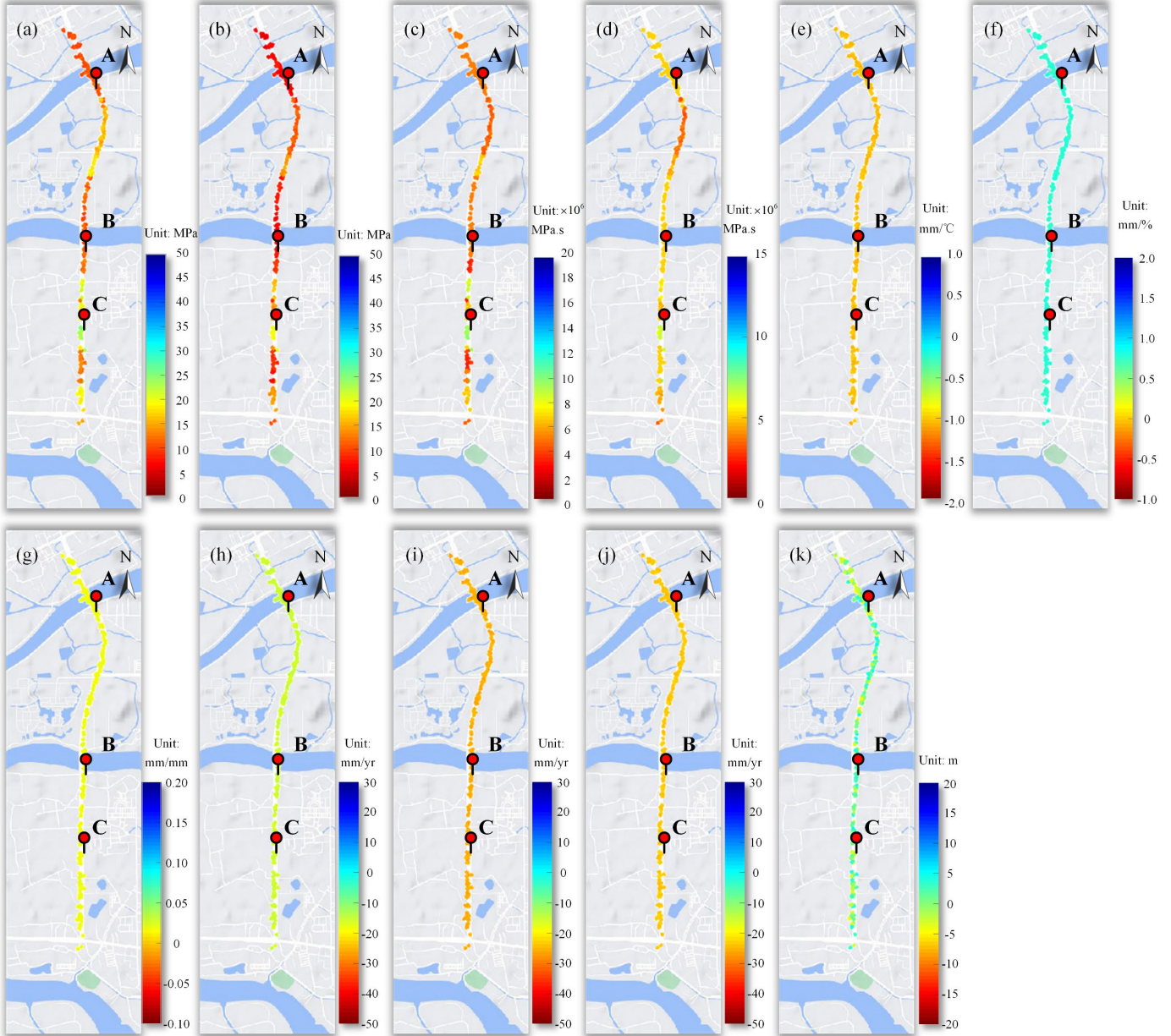


Fig. 8. Estimated model parameters for GH (the points A-C are the selected feature points): (a) E_1 ; (b) E_2 ; (c) η_1 ; (d) η_2 ; (e) α_1 ; (f) α_2 ; (g) α_3 ; (h) v_1 ; (i) v_2 ; (j) v_3 ; (k) Δz .

The GH is in the suburban area of the Shunde District, surrounded by extensive ponds and waterways. We can see from Fig. 11 that the spatial-temporal distribution of the GH is similar to that of the LH. In terms of the spatial distribution, the large subsidence area is close to the waterways, while the

deformation in the inland area is relatively slow. In addition, two distinct subsidence funnels, marked as purple rectangles G1 and G2 in Fig. 11, were detected. G1 is at the juncture of G105 and GH, and G2 is around the junction of the S39 Highway and GH (the locations of G105 and S39 are shown in Fig. 12). The

most obvious subsiding area is G2, with a maximum deformation of -158 mm in January 2017. Temporally, a similar subsiding trend with periodic fluctuations dominated this area, with the maximal localized settlement reaching 158 mm on

January 14, 2017. Distinct jumps were then detected for three periods in this area: March 08, 2015, to May 13, 2015; November 27, 2015, to January 10, 2016; and July 04, 2016, to September 08, 2016, with a maximum recovery of 55 mm.

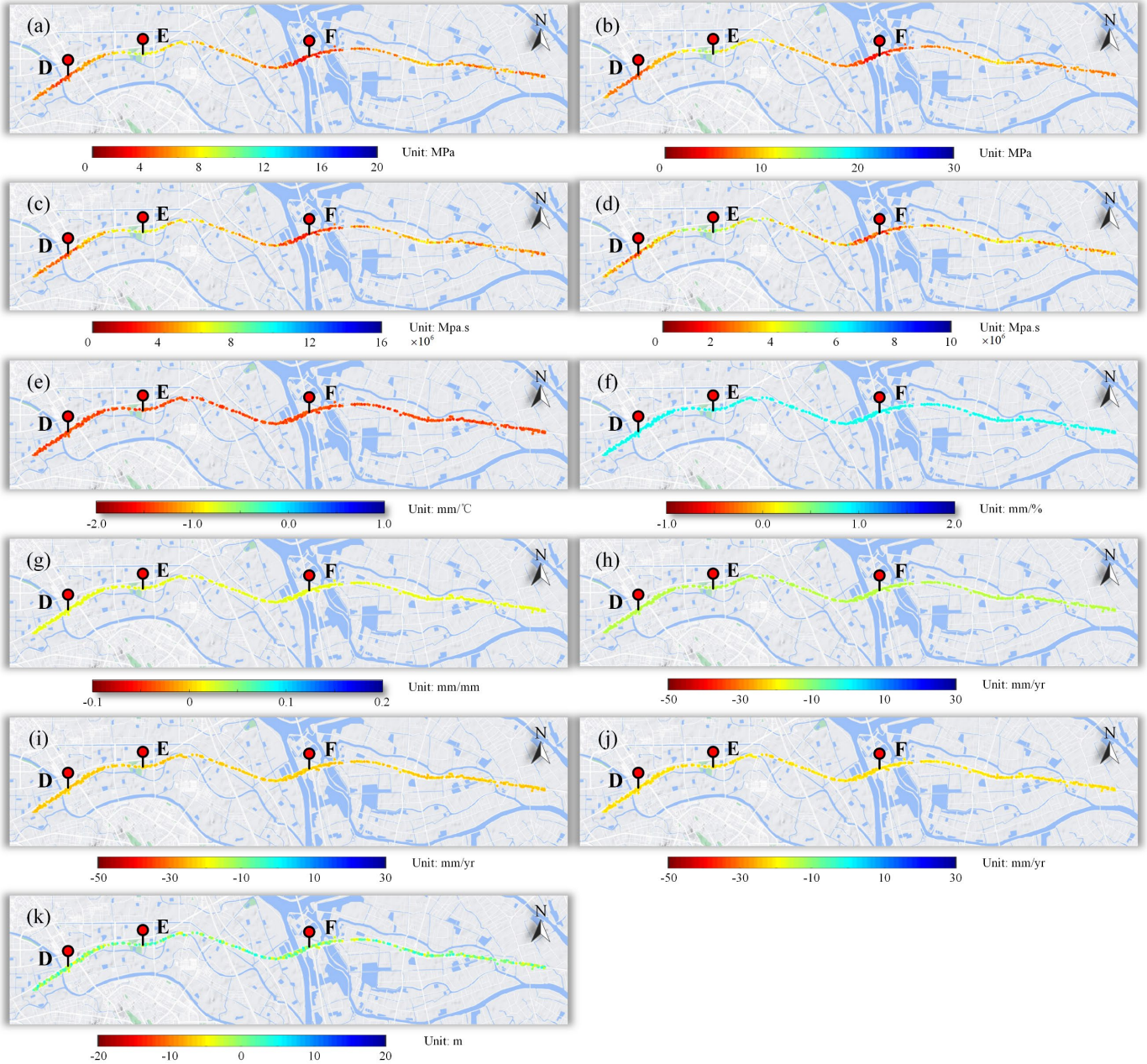


Fig. 9. Estimated model parameters for GH (the points D-F are the selected feature points): (a) E_1 ; (b) E_2 ; (c) η_1 ; (d) η_2 ; (e) α_1 ; (f) α_2 ; (g) α_3 ; (h) v_1 ; (i) v_2 ; (j) v_3 ; (k) Δz .

3) Deformation characteristics over feature points: To reveal the temporal characteristics of the generated deformation, six feature points located in the riverside area (marked as A and B in Fig. 8), the inland area (marked by C and E in Fig. 8 and Fig. 9) and the subsidence funnels (marked as D and F in Fig. 9) were extracted. As shown in Fig. 12, A is located in the riverside area close to the Shunde Tributary Channel, B is close to the Ronggui Waterway, C is near Junye Road, D is at the

intersection of GH and G105 Highway, E is at the intersection of GH and Xinji Road, and F is at the junction of GH and S39 Highway. Fig. 12 shows the annual average deformation velocity of each feature point, where the velocity of point A is -48 mm/yr, B is -45 mm/yr, C is -19 mm/yr, D is -60 mm/yr, E is -21 mm/yr, and F is -78 mm/yr. The corresponding time-series deformation at each point is then shown in Fig. 13.

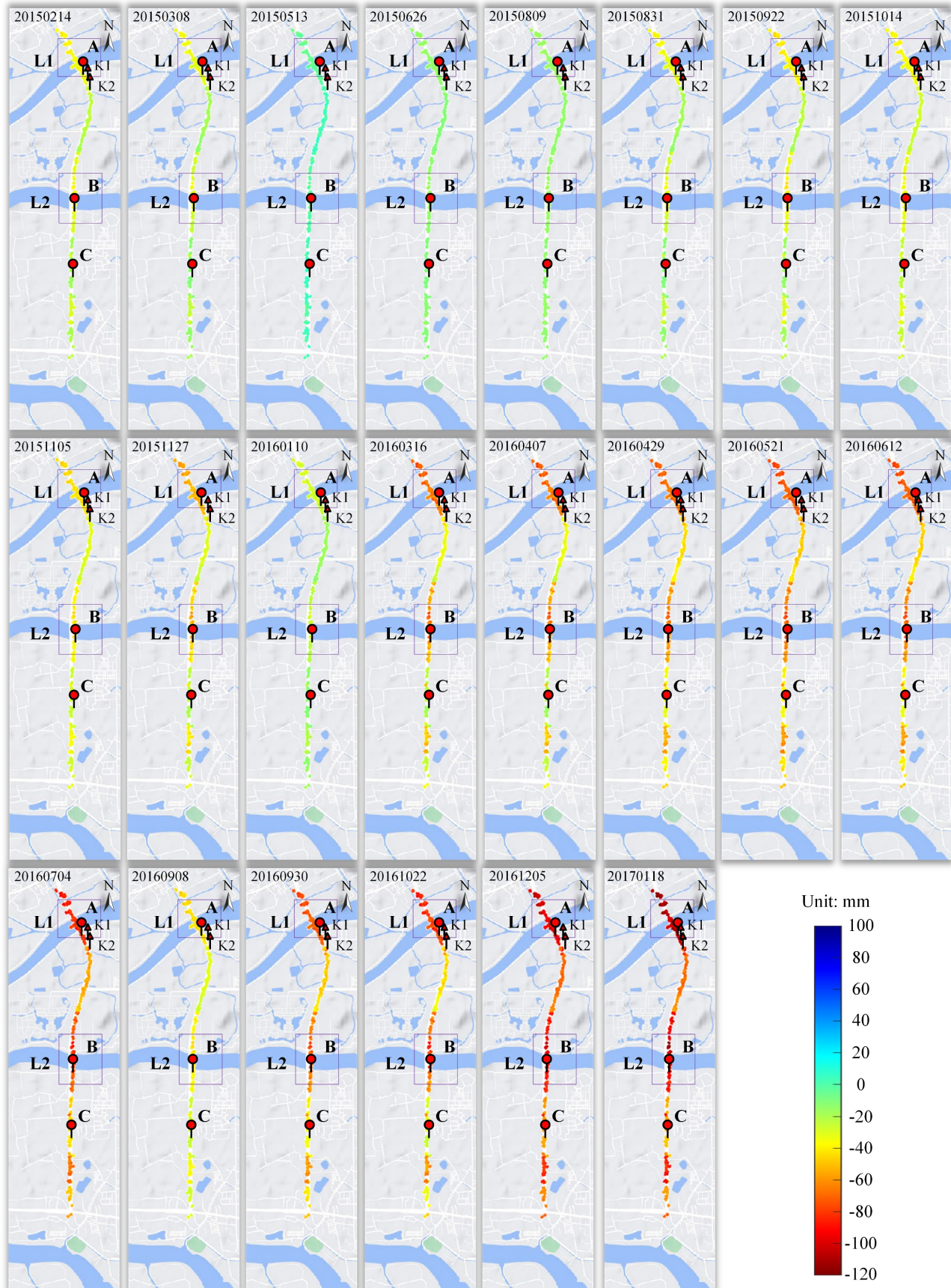


Fig. 10. Generated deformation sequences of the LH (with reference to 01/01/2015; A-C represent the locations of feature points; K1 and K2 are the benchmarks).



Fig. 11. Generated deformation sequences of the GH (with reference to 01/01/2015; D-F represent the locations of feature points).

We can see that the observed total surface deformation over the six points showed a general subsidence trend with similar seasonal variations. These patterns are mainly related to the rheological properties and external environmental factors (which will be discussed in Section V in detail). In the time sequence, there were some distinct uplifts in the surface deformation for all six feature points. Taking point F as an example, noticeable uplifts of 13 mm, 20 mm, and 55 mm occurred during the periods from March 08 to May 13, 2015, November 27, 2015, to January 10, 2016, and July 04 to September 08, 2016, respectively.

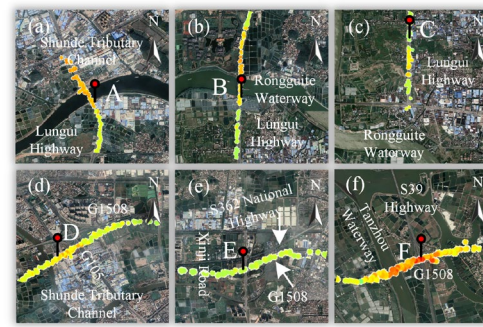


Fig. 12. Annual average deformation velocities and the locations of each feature point on Google Maps.

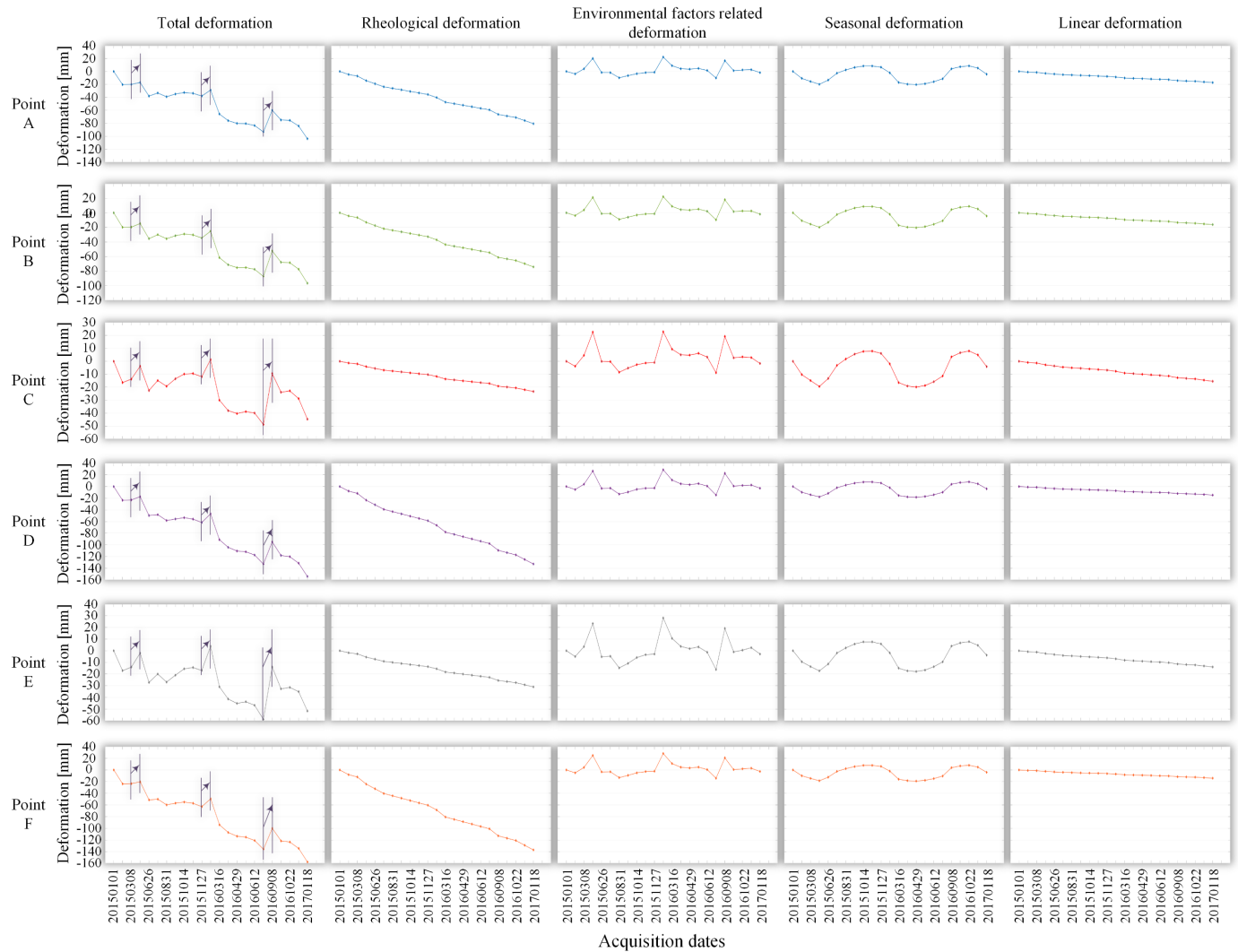


Fig. 13. Temporal evolution of the deformation components (total, rheological, environmental factors related, seasonal, and linear deformation) at the six feature points.

The total temporal deformation of each feature point mainly includes four components (as shown in Fig. 13), including the component related to rheological properties, environmental factors, the seasonal component, and the linear component. Table II lists the proportion of each component, from which we

can see that the rheological deformation accounted for the maximum percentage of the total deformation, indicating that the deformation in the area was most considerably affected by the rheological properties.

TABLE II
THE PROPORTION OF EACH DEFORMATIONAL COMPONENT ON THE FEATURE POINTS

Deformation component	Feature points					
	A	B	C	D	E	F
Rheological component	62.7%	61.0%	33.7%	73.9%	40.5%	74.6%
Seasonal component	8.8%	9.3%	17.3%	8.2%	18.9%	7.8%
Environmental component	15.3%	16.4%	26.5%	9.8%	22.4%	9.9%
Linear component	11.8%	12.0%	19.3%	6.5%	14.1%	5.6%
Residual component	1.4%	1.3%	3.2%	1.6%	4.1%	2.1%

4) Accuracy validation: As introduced in [14], the HP deformation extracted from the residual phases can be used to evaluate the accuracy for a deformation model in InSAR time-series modelling. The average HP deformation for each interferogram obtained through NREM, KM, conventional linear model (LM), and seasonal model (SM) are exhibited in Fig. 14. Obviously, we can see that the overall magnitude of the NREM is smaller than that of the other models, indicating that the NREM is most suitable for surface monitoring in our cases. For LH, the standard deviations (STDs) of the HP deformation obtained by the NREM are ± 2.7 mm (as shown in Fig. 14), with an improvement of 44.9% compared to that of the LM. For GH, the STDs of the HP deformation over all interferograms acquired by the NREM are ± 2.2 mm, whereas that of the LM is ± 4.6 mm, achieving an increase of 50%.

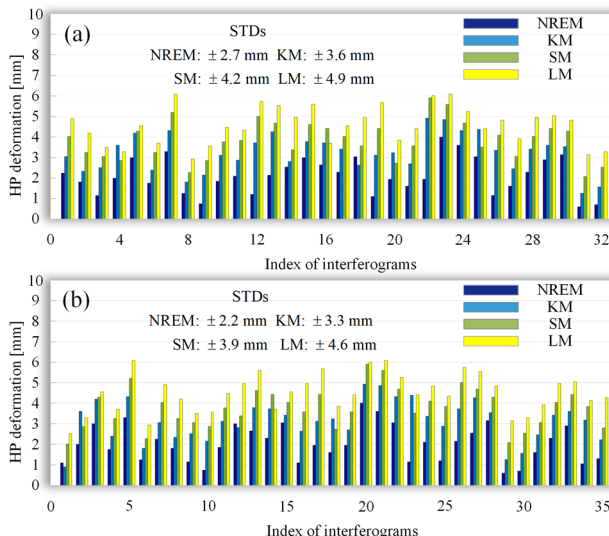


Fig. 14. HP deformation comparison: (a) Lungui Highway; (b) G1508 Highway.

Ground levelling measurements from 10 July 2016 to 8 January 2017 were collected to verify the InSAR results for LH

(the two levelling points are shown in Fig. 10, marked as K1 and K2). The quantitative comparison between the levelling measurements and the InSAR results on the benchmarks is shown in Fig. 15, with the comparison results of the RMSEs. From Fig. 15 we can see that the uplift between August 24, 2016 to September 8, 2016 (with 5.5 mm's discrepancy with leveling results for NREM) was not detected in the leveling results, but was detected for all the results generated by the four models. The reason for the discrepancy with leveling results are suggested related to the residual atmospheric delay and orbit errors which still existed in the processing results (Although the polynomial fitting method for orbit errors [39] and temporal-spatial HP-LP filtering for residual atmospheric delay [40] have been adopted to eliminate their influences in the interferometric processing).

As shown in Fig. 15, the obtained RMSEs of K1 generated by NREM accounts for 12.3% relative to the total accumulated deformation of 50 mm, and 5% for K2. With reference to the previous work [41, 42], the relative errors (12.3% for K1 and 5% for K2) in this work are in an acceptable range. As expected, the deformation derived by NREM has the lowest RMSEs of ± 5.1 mm among the four models, with an improvement of approximately 41% compared to that of LM.

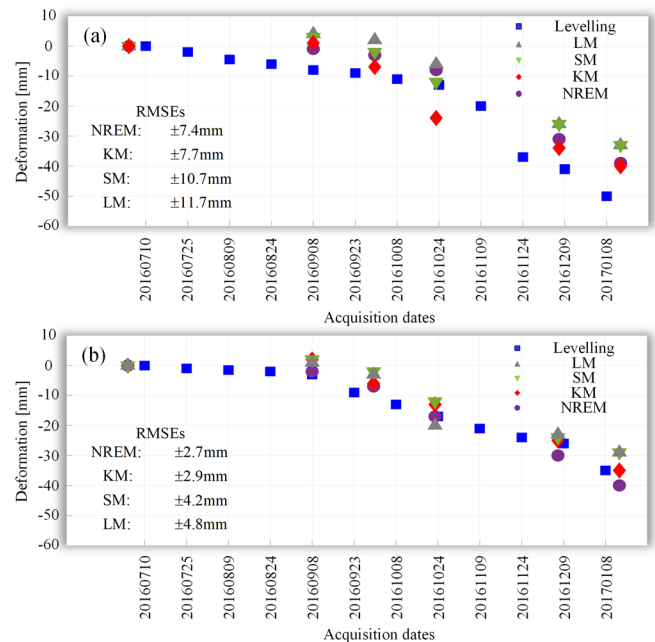


Fig. 15. Comparison with levelling measurements on benchmarks: (a) K1; (b) K2.

V. DISCUSSIONS

A. Suggested reasons for the subsidence

The suggested reasons for the generated subsidence are as follows:

1) We found an interesting phenomenon according to Fig. 8 to Fig. 11: the lower the value of the rheological parameters, the higher the deformation. Rheological properties are one of the important geotechnical characteristics of soft soil and define the phenomenon of soil deformation related to time. According to Eq. (2), when the external stress is considered constant, the elastic stress is inversely proportional to the deformation [43].

Comparatively, viscosity is an expression of the fluid flow dynamics for the inner frictional phenomenon of a fluid [44], where a high viscosity reflects a high internal friction. Consequently, viscosity can be understood as a physical quantity that describes the internal friction property of soil particles, mainly reflecting the ability of soil to resist deformation. A higher viscosity indicates that the friction resistance between the soil particles is large, which means that strain and deformation do not easily occur. As a result, the region with a lower deformation had higher elastic modulus and viscosity magnitudes.

2) As discussed in Section IV-C, we determined that the overall accumulated deformation was characterized by a completely subsiding trend with periodical variations. In the plain area, quaternary sediments can be allocated into four aquifers in the vertical direction. The first aquifer primarily exists in the alluvial fan underpart, whose lithology includes sandy sand, fine sand, and silty sand. Groundwater recharge generally comes from the supply of precipitation, irrigation, and river infiltration. The second aquifer, containing various types of gravel, soft clay, and sand, was recharged from the first aquifer due to leakage of the groundwater extraction. The third aquifer, with a lithology similar to that of the second aquifer, accepts infiltration and lateral supply. The fourth aquifer, whose lithology is mainly sand, was under a weak hydraulic relationship with the upper aquifer [45]-[48]. With an increasing precipitation and a drop in the external temperature, the groundwater in the first aquifer will evidently rise, leading to the uplift phenomenon on the ground surface. Subsequently, the recharge supply to the second and third aquifers will increase accordingly, which will also contribute to the apparent uplift of the surface. Conversely, when the temperature increases and the precipitation decreases, the surface deformation is mainly in the form of subsidence [49]. The humidity was affected by the combined temperature and precipitation, which decreased with an increase in the temperature and a decrease in the rainfall. Fig. 6 shows information on the air temperature, monthly total precipitation, and monthly average humidity of the Shunde District from January 2015 to January 2017. From April to May 2015, although a 4 °C increase in temperature occurred, a 1300 mm increase in precipitation eventually led to a 15% increase in humidity. Similarly, for the two uplift periods shown in Fig. 13 (December 2015 to January 2016 and July 2016 to August 2016), increments of 3% and 2% of the humidity were induced by the 400 mm and 1100 mm increments of the monthly total precipitation, respectively. This could be responsible for the uplift of the surface deformation.

B. Rheological properties analysis

Generally, the settlement process of soft soil consists of three stages for highway engineering, i.e., instant settlement (S_d), primary consolidation settlement (S_c), and secondary consolidation settlement (S_s), which is also called rheological deformation. The former two stages mainly occur in the construction stage of the highway. Since long-term monitoring is performed for the postconstruction settlement of the two test highways, we focus on the interpretation of S_s here. Based on the rheological mechanism of soft soil, the water and gas in the pore space are partially squeezed out under the action of the

external force. Then, rearrangement of the inner soil particles occurs, which leads to deformation of the soil skeleton. On the one hand, the discharge of fluid is hindered by the friction between soil particles and the pore fluid, leading to the delay of soil deformation. On the other hand, the soil deformation is also delayed by the viscosity of the film, since the contact among the soil particles is based on the contact of the hydrated water film, which leads to a significant time effect of the rheological deformation of soft clay. As introduced in II-A, we only pay attention to the rheological properties of soil induced by vertical compression, and the external stress σ_c is assumed to be constant.

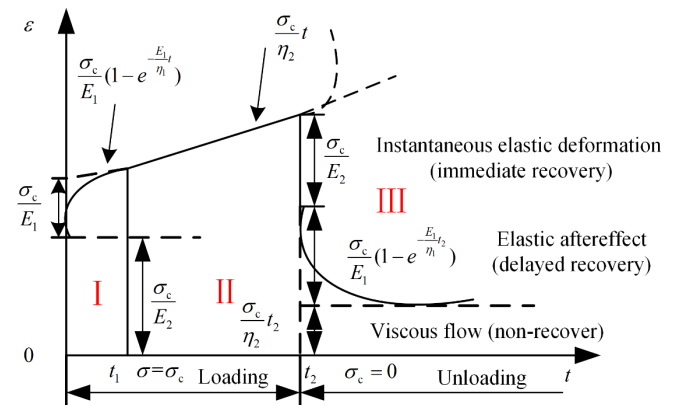


Fig. 16. The rheological curve of the Burgers model [26].

In this work, the BM is selected to model the rheological components. The BM is constructed through a connection series of Maxwell and Kelvin bodies. The rheological curve of the Burgers model is represented in Fig. 16. The rheological characteristics for the two highways can be revealed by the rheological curves over the six feature points, as shown in Fig. 17. The rheological curve can show the temporal relationship of ϵ and can assist us in further revealing the deformation disciplines for the soil. This is commonly used in the geotechnical highway engineering field. The functional relationship between the stress and the strain for the curves in Fig. 16 at $t = 0$ follows equation $\epsilon = \frac{\sigma_c}{E_2}$, and is highly related to the nature of the materials. This is called instantaneous elastic deformation, indicating the property where the spring will instantly generate elastic displacement at the moment of loading. In the rheological behaviour stage (also called secondary consolidation) of soft clay, two temporal periods (marked as I and II in Fig. 16) mainly dominate the total period of deformation. The first period, namely, the accelerated creeping stage, is shown as the 0 to t_1 period when the deformation increases nonlinearly with time, following the function $\epsilon = \frac{\sigma_c}{E_1} (1 - e^{\frac{E_1 t_1}{\eta_1}})$. The second period, namely, the constant velocity creep, is shown as the t_1 to t_2 period. The deformation during this stage increases linearly with time, following the viscous flow function $\epsilon = \frac{\sigma_c}{\eta_2} t$. When $t = t_2$ and $\sigma = 0$, which is called the unloading moment, the instantaneous elastic deformation instantly recovers, releasing the viscous flow part. The period 0 – t_2 for the postconstruction step of highways is the focus here.

TABLE III
RHEOLOGICAL PARAMETERS OF EACH FEATURE POINT

Feature points	Rheological parameters			
	E_1 (MPa)	E_2 (MPa)	η_1 (10^6 MPa.s)	η_2 (10^6 MPa.s)
A	6.9730	7.9210	4.2160	4.5532
B	9.0688	11.9242	4.8436	5.0672
C	23.0122	18.0222	9.7293	6.3170
D	4.1582	7.2981	2.6135	2.3382
E	18.3050	12.9542	5.9288	6.0170
F	4.0289	6.8893	1.0735	1.7550

As discussed above, we draw the creep curve of each feature point according to (1), which is shown in Fig. 17. The creep curves for the six feature points present similar temporal variation characteristics. The ideal strain at each high coherence point in the test highways can be estimated according to (1). Each rheological parameter of the six feature points is listed in Table III. Taking point A located in the LH area as an example, the estimated elastic modulus E_1 is 6.97 MPa, the elastic modulus E_2 is 7.92 MPa, the viscosity η_1 is 4.22×10^6 MPa.s, and the viscosity η_2 is 4.55×10^6 MPa.s. As presented in Fig. 17, an instantaneous elastic modulus appeared at A with a strain of 0.3 at moment $t = 0$. Then, an acceleration period of the strain began until $t = 220$ days (marked as the first black dotted line in Fig. 17), and the slope of the curve reached equilibrium and changed linearly with time. Its strain accumulated to 3.5 until January 2017 (748 days). For point B, the acquired rheological parameters were 9.07 MPa, 11.92 MPa, 4.84×10^6 MPa.s, and 5.07×10^6 MPa.s, respectively, with a cumulative strain of 3.2 on January 2017 (748 days). The total variations in the creep curves drawn from the InSAR estimated results show good consistency with those shown in Fig. 16, which indicates that the estimated rheological parameters and the creep curves can reflect the physical rheological properties of the soil in the study areas.

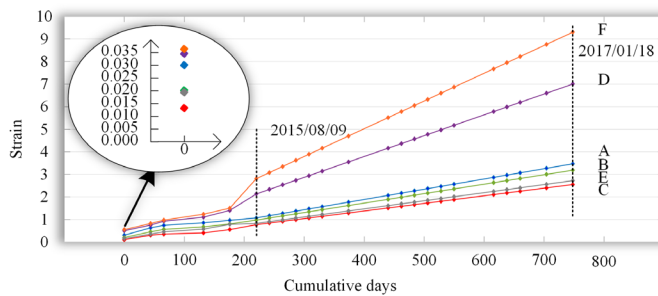


Fig. 17. The rheological curves (strain-time curve) over the six feature points.

As discussed above, we draw the creep curve of each feature point according to (1), which is shown in Fig. 17. The creep curves for the six feature points present similar temporal variation characteristics. The ideal strain at each high coherence

point in the test highways can be estimated according to (1). Each rheological parameter of the six feature points is listed in Table III. Taking point A located in the LH area as an example, the estimated elastic modulus E_1 is 6.97 MPa, the elastic modulus E_2 is 7.92 MPa, the viscosity η_1 is 4.22×10^6 MPa.s, and the viscosity η_2 is 4.55×10^6 MPa.s. As presented in Fig. 17, an instantaneous elastic modulus appeared at A with a strain of 0.3 at moment $t = 0$. Then, an acceleration period of the strain began until $t = 220$ days (marked as the first black dotted line in Fig. 17), and the slope of the curve reached equilibrium and changed linearly with time. Its strain accumulated to 3.5 until January 2017 (748 days). For point B, the acquired rheological parameters were 9.07 MPa, 11.92 MPa, 4.84×10^6 MPa.s, and 5.07×10^6 MPa.s, respectively, with a cumulative strain of 3.2 on January 2017 (748 days). The total variations in the creep curves drawn from the InSAR estimated results show good consistency with those shown in Fig. 16, which indicates that the estimated rheological parameters and the creep curves can reflect the physical rheological properties of the soil in the study areas.

C. Correlation analysis of the external environmental factors

To further investigate the correlation between the external environmental factors (i.e., the temperature, humidity, and precipitation) and the generated ground deformation in the soft clay area, a correlation analysis over all the high coherence points was conducted. The detailed analysis at the six selected feature points with respect to temperature, humidity, and precipitation are shown in Fig. 18(a) to (c), and the statistical histograms of the correlation analysis over all the high coherence points on each external environmental parameter are represented in Fig. 18(d) to (e). The deformation over the six selected feature points was negatively correlated with the monthly average temperature, but was positively related to both the humidity and the total precipitation, as exhibited in Fig. 16. As mentioned in IV-C, the three detected uplift periods are marked in Fig. 18(a)-(c), which can help us understand the suggested reasons introduced in IV-C for the uplifts related to the drop in temperature and the large increment in precipitation. As shown in Fig. 18(d) and (e), the statistical curves for the two test highways show that the correlation coefficients completely ranged from -0.85 to -0.45, and that the majority of the correlation coefficients were mainly concentrated at -0.65. This indicates that the ground surface deformation over the two soft clays was moderately correlated to the air temperature. In contrast, the time-series deformation was positively related to both precipitation and humidity. The deformation was also strongly related to the precipitation (up to 0.70) but weakly related to the humidity (only 0.21).

D. Sensitivity analysis on the NREM parameters

As discussed in [16], the accuracies of the InSAR-generated deformations are highly correlated with the accuracies of the estimated model parameters. Through a sensitivity analysis of the model parameters, we can determine which parameters have a more significant impact on the overall output and dynamic variations of the NREM. Ten groups of inaccurate NREM parameters were generated in the simulation. The simulated values and the error ranges are listed in Table IV.

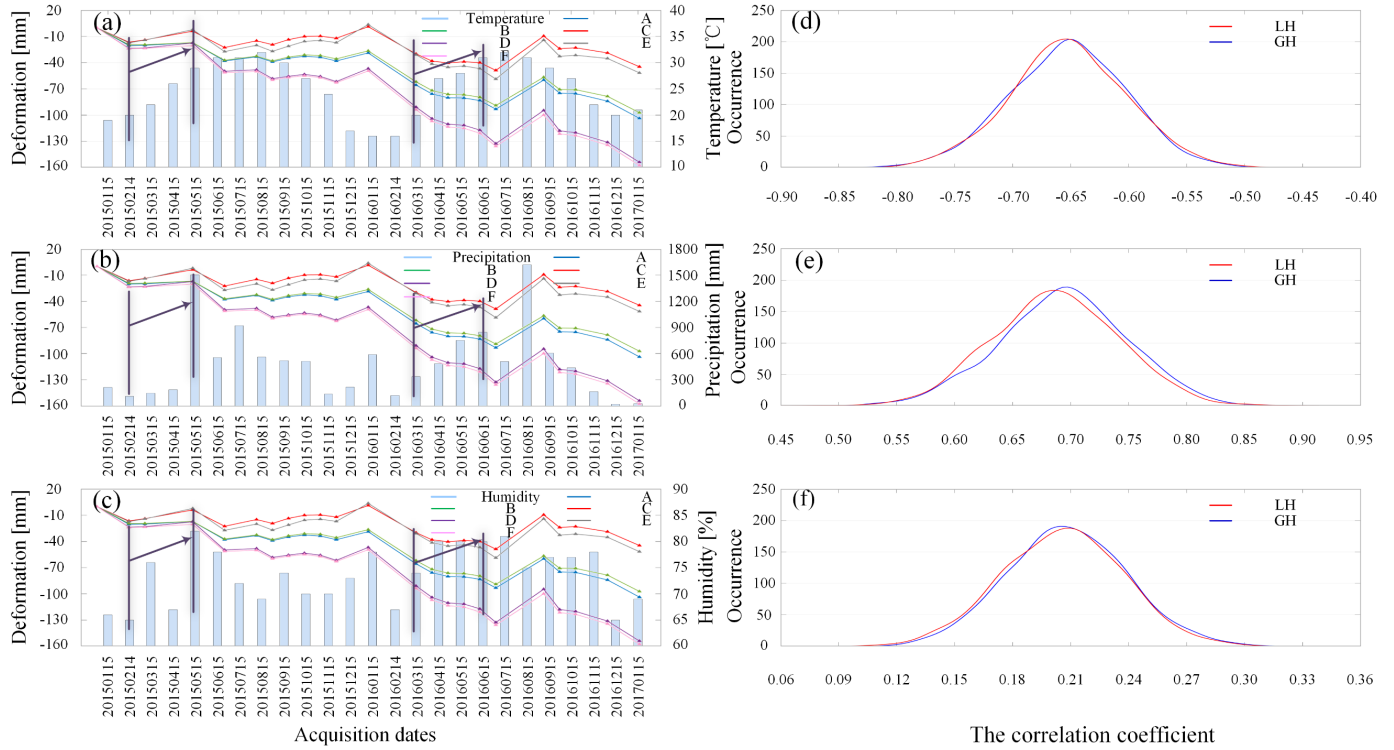


Fig. 18. Correlation analysis between the time-series deformation and the external environmental factors: (a)-(c) detailed correlation analysis at the feature points; (d)-(f) histograms of the correlation coefficients.

TABLE IV

INACCURACY RANGES OF THE NREM PARAMETERS

NREM parameters	Sensitivity analysis		
	I	Ranges of I'	Simulated inaccuracy
E_1 (MPa)	10	4 – 16	-60% – 60%
E_2 (MPa)	25	20 – 30	-20% – 20%
η_1 (10^6 MPa.s)	5	0 – 10	-100% – 100%
η_2 (10^6 MPa.s)	10	5 – 15	-50% – 50%
α_1 (mm/°C)	-1	-0.6 – 1.4	-40% – 40%
α_2 (mm/%)	1	0.5 – 1.5	-50% – 50%
α_3 (mm/mm)	0.05	0.03 – 0.07	-40% – 40%
v_1 (mm/yr)	-50	-100 – 0	-100% – 100%
v_2 (mm/yr)	-20	-40 – 0	-100% – 100%
v_3 (mm/yr)	-20	-40 – 0	-100% – 100%

Fig.19 shows the sensitivity results for NREM. The corresponding error of the vertical subsidence D is determined by $D/D_{\max} \times 100\%$, where D_{\max} is the maximum subsidence in the region. The deformation error induced by inaccurate NREM parameters was generally symmetric along the positive and negative directions. As inferred from Fig.19, the NREM-estimated deformation was highly sensitive to parameters E_2 and η_2 , which indicates that the rheological characteristics dominate the deformation of the test soft clays. Comparatively, E_1 and η_1 showed limited influences on the final deformation among the four rheological parameters. Compared with the influences of the rheological parameters, the effects of the other parameters are much limited. Among the remaining parameters, the environmental parameters present the highest sensitivity, followed by the seasonal parameters and the linear velocity, which is consistent with the discussions in Section IV. Consequently, we should pay more attention to the accuracy of the NREM parameters, especially the rheological

parameters, in order to precisely predict the highway deformation over soft clay subgrades and prevent highways from transportation safety accidents.

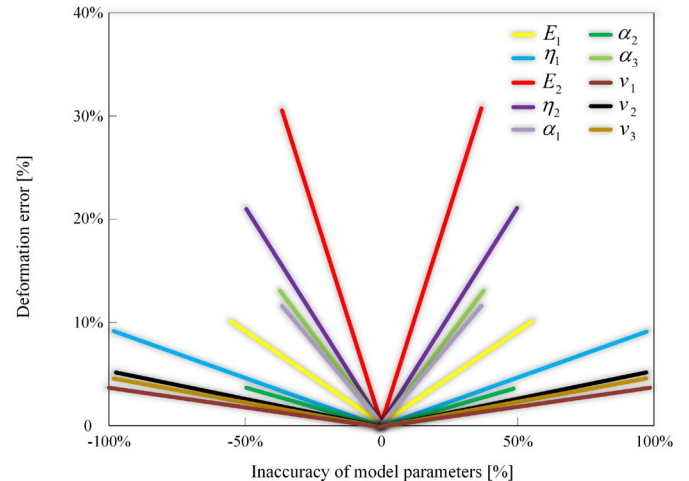


Fig. 19. Results of the sensitivity analysis for NREM.

VI. CONCLUSIONS

In this work, a novel InSAR deformation model (NREM) that considers the rheological properties and environmental factors was proposed to overcome the limitations of traditional InSAR deformation models. The Burgers model from the field of rheology was introduced into the traditional seasonal model to improve the accuracy of the estimated time-series deformation and better interpret the influence of the rheological properties on the surface deformation over the highway area built on soft soil foundations. The combination of GA and the Simplex

Algorithm (SA), namely GA-SA, was employed to estimate the model parameters. With the use of 23 TerraSAR X-band Stripmap images, the time-series deformation based on the NREM was generated, and the estimations for the primary rheological—parameters, i.e., the elastic modulus and viscosity, were acquired by our InSAR-based measurements, which can provide a reference for the highway engineering field. The rheological properties of the study area were also revealed according to the estimated rheological parameters and the time-series deformation results. The maximum deformation of -158 mm in January 2017 and three periods of seasonal uplifts with a maximum subsidence recovery of 55 mm were temporally detected. The suggested reasons for the variations were related to the significant increase in precipitation and the decrease in temperature. Spatially, the deformation is generally inversely proportional to the value of the viscosity and the elastic modulus.

To evaluate the reliability of the results obtained by the NREM, the STDs of HP deformation generated by the NREM were calculated, and the results showed that the NREM-generated results were reduced by 44.9% for the LH area and 50% for the GH area, compared to conventional deformation models. The accuracy for the LH was also evaluated by the in situ levelling measurements, and the average RMSEs for NREM results were estimated as ± 5.1 mm, which was obviously lower than that of the traditional models. A correlation analysis on the external environmental factors was executed to further investigate the correlation between the external environmental factors and the deformation. It was determined that the deformation was negatively correlated with the temperature and positively correlated with the precipitation and humidity.

The method proposed in this work still has some weaknesses. First, we treated the external load as constant in the time-series, ignoring the influence of the periodical load of the vehicles. Second, in addition to the external physical factors, the internal physical factors of soft clay, such as the void ratio and the compression ratio, also have a great influence on the deformation. Henceforth, we will be involved in introducing the periodical dynamic parameters and the internal physical factors of soft clay into the NREM.

ACKNOWLEDGMENT

The TerraSAR-X satellite images used in this work are provided by the Deutsches Zentrum für Luftfahrt und Raumfahrt (DLR) (Dara Order Program Project: MTH3393, LAN3663). Thanks for Professor Zhang J.H. of Transportation Engineering College, Changsha University of Science and Technology, China for providing the levelling deformation data of Lungui Highway, which provides available validation data for this work.

REFERENCES

- [1] L. Y. Pan, and X. Y. Xie, "Observational settlement prediction by curve fitting methods," (in Chinese), *Rock Soil Mech.*, vol. 25, no.7, pp. 1053-1058, Jul. 2004.
- [2] C. E. Hunt, J. M. Pestana, J. D. Bray, and M. Riemer, "Effect of pile driving on static and dynamic properties of soft clay," *J. Geotech. Geoenviron. Eng.*, vol. 128, no. 1, pp. 13-24, Jan. 2002.
- [3] X. G. Shi, M. Liao, J. C. Wang, M. Zhang, and W. Shan, "Expressway deformation mapping using high-resolution TerraSAR-X images," *Remote Sens. Lett.*, vol. 5, no. 2, pp. 194-203, Jul. 2014.
- [4] A. Ferretti, C. Prati, and F. L. Rocca, "Permanent scatterers in SAR interferometry," *IEEE Trans. Geosci. Remote Sens.*, vol. 39, no. 1, pp. 8-20, 2001.
- [5] P. Berardino, G. Fornaro, R. Lanari, and E. Sansosti, "A new algorithm for surface deformation monitoring based on small baseline differential SAR interferograms," *IEEE Trans. Geosci. Remote Sens.*, vol. 40, no. 11, pp. 2375-2383, Nov. 2002.
- [6] X. Q. Qin, M. S. Liao, L. Zhang, and M. S. Yang, "Structural health and stability assessment of high-speed railways via thermal dilation mapping with time-series InSAR analysis," *IEEE J. Sel. Top. Appl. Earth Observ. Remote Sens.*, vol. 10, no. 6, pp. 2999-3010, Jul. 2017.
- [7] X. Q. Qin, L. Zhang, M. S. Yang, H. Luo, and M. S. Liao, "Mapping surface deformation and thermal dilation of arch bridges by structure-driven multi-temporal DInSAR analysis," *Remote Sens. Environ.*, vol. 216, pp. 71-90, Oct. 2018.
- [8] R. Wang, T. L. Yang, M. S. Yang, M. S. Liao, and J. X. Lin, "A safety analysis of elevated highways in Shanghai linked to dynamic load using long-term time-series of InSAR stacks," *Remote Sens. Lett.*, vol. 10, no. 12, pp. 1133-1142, Aug. 2019.
- [9] E. A. Hetland, P. Musé, M. Simons, Y. N. Lin, P. S. Agram, and C. J. DiCaprio, "Multiscale InSAR time series (MInTS) analysis of surface deformation," *J. Geophys. Res.-Solid Earth*, vol. 117, no. B2, pp. 1-17, Feb. 2012.
- [10] B. M. Kampes and R. F. Hanssen, "Ambiguity resolution for permanent scatterer interferometry," *IEEE Trans. Geosci. Remote Sens.*, vol. 42, no. 11, pp. 2446-2453, Nov. 2004.
- [11] S. Kim, S. Wdowinski, T. H. Dixon, F. Amelung, J. W. Kim, and J. S. Won, "Measurements and predictions of subsidence induced by soil consolidation using persistent scatterer InSAR and a hyperbolic model," *Geophys. Res. Lett.*, vol. 37, no. 5, Mar. 2010.
- [12] C. Colesanti, A. Ferretti, F. Novali, C. prati, and F. Rocca, "SAR monitoring of progressive and seasonal ground deformation using the permanent scatterers technique," *IEEE Trans. Geosci. Remote Sens.*, vol. 41, no. 7, pp. 1685-1701, Jul. 2001.
- [13] X. M. Xing, L. F. Chen, Z. H. Yuan, and Z. N. Shi, "An improved time-series model considering rheological parameters for surface deformation monitoring of soft clay subgrade," *Sensors*, vol. 19, no.14, pp. 3073, Jul. 2019.
- [14] R. Zhao, Z. W. Li, G. C. Feng, Q. J. Wang, and J. Hu, "Monitoring surface deformation over permafrost with an improved SBAS-InSAR algorithm: With emphasis on climatic factors modeling," *Remote Sens. Environ.*, vol. 184, pp. 276-287, Oct. 2016.
- [15] C. Wang, Z. J. Zhang, H. Zhang, Q. B. Wu, B. Zhang, and Y. X. Tang, "Seasonal deformation features on Qinghai-Tibet railway observed using time-series InSAR technique with high-resolution TerraSAR-X images," *Remote Sens. Lett.*, vol. 8, pp. 1-10, Sep. 2016.
- [16] Z. Yang, Z. W. Li, J. J. Zhu, J. Hu, G. Feng, Y. Wang, and M. Papast, "An InSAR-based temporal probability integral method and its application for predicting mining-induced dynamic deformations and assessing progressive damage to surface buildings," *IEEE J. Sel. Top. Appl. Earth Observ. Remote Sens.*, vol. 11, no. 2, pp. 472-484, Feb. 2018.
- [17] W. H. Gao and P. S. Shen, "Influence on strata deformation for staged construction of excavation in soft clay," (in Chinese), *J. Xiangtan Min. Inst.*, vol. 17, no. 1, pp. 1-4, 2002.
- [18] D. A. Sun and H. E. Shen, "Experimental study on rheology behaviour of Shanghai soft clay," *Hydrogeol. Eng. Geol.*, vol. 37, no.3, pp. 74-78, 2010.
- [19] M. K. Huang, *Highway engineering material rheology*, (in Chinese). Chengdu, China: Southwest Jiaotong University Press, 2010.
- [20] X. W. Zhang, C. M. Wang, "Viscosity coefficient of structural soft clay," (in Chinese), *Rock Soil Mech.*, vol. 32, no.11, pp. 3276-3282, Nov. 2011.
- [21] X. Xing, H.-C. Chang, L. Chen, J. Zhang, Z. Yuan, and Z. Shi, "Radar Interferometry Time Series to Investigate Deformation of Soft Clay Subgrade Settlement—A Case Study of Lungui Highway, China," *Remote Sens.*, vol. 11, no. 4, pp. 429, Feb. 2019.
- [22] S. L. Gong, C. Li, and S. L. Yang, "The microscopic characteristics of Shanghai soft clay and its effect on soil body deformation and land subsidence," *Environ. Geol.*, vol. 56, pp. 1051-1056, Feb. 2008. DOI: 10.1007/s00254-008-1205-4.
- [23] Y. K. Zhu, X. X. Xing, L. F. Chen, Z. H. Yuan, and P. Y. Tang, "Ground Subsidence Investigation in Fuoshan, China, Based on SBAS-InSAR Technology with TerraSAR-X Images," *Appl. Sci.*, vol. 9, no. 10, pp. 2038, May. 2019.

- [24] X. B. Li, *Theoretical and experimental studies on rheological consolidation of soft soil*, (in Chinese). Zhejiang University, 2005.
- [25] J. M. Carcione, and F. Poletto, "Seismic rheological model and reflection coefficients of the brittle–ductile transition," *Pure Appl. Geophys.*, vol. 170, no. 12, pp. 2021-2035, Feb. 2013.
- [26] B. W. Zhao, *Consolidation and rheology for soft clay*, (in Chinese). Nanjing, China: Hohao University Press, 1996.
- [27] S. S. Li, Z. W. Li, J. Hu, Q. Sun, and X. Y. Yu, "Investigation of the seasonal oscillation of the permafrost over qinghai-tibet plateau with sbas-inSAR algorithm," *Chin. I. Geophys.*, vol. 56, no. 5, pp. 1476-1486, May. 2013.
- [28] Y. Xu, L. Ma, Y. Du, and S. Shen, "Analysis of urbanisation-induced land subsidence in Shanghai," *Nat. Hazards*, vol. 63, no. 2, pp. 1255-1267, May. 2012.
- [29] C. Zhou, H. Gong, B. Chen, J. Li, M. Gao, F. Zhu, W. Chen, and Y. Liang, "InSAR time-series analysis of land subsidence under different land use types in the eastern Beijing plain, China," *Remote Sens.*, vol. 9, no. 4, pp. 380, Apr. 2017.
- [30] J. Hu, J. Liu, Z. Li, J. Zhu, L. Wu, Q. Sun, and W. Wu, "Estimating three-dimensional coseismic deformations with the SM-VCE method based on heterogeneous SAR observations: Selection of homogeneous points and analysis of observation combinations," *Remote Sens. Environ.*, vol. 255, Mar. 2021.
- [31] Z. F. Yang, Z. W. Li, J. J. Zhu, H. W. Yi, J. Hu, and G. C. Feng, "Deriving dynamic subsidence of coal mining areas using InSAR and logistic model," *Remote Sens.*, vol. 9, no. 2, pp. 125, Feb. 2017.
- [32] G. R. Liu, X. Han, and K. Y. Lam, "A combined genetic algorithm and nonlinear least squares method for material characterization using elastic waves," *Comput. Method. Appl. M.*, vol. 191, no. 17/18, pp. 1909-1921, Feb. 2002.
- [33] L. Yao, W. A. Sethares, "Nonlinear parameter estimation via the genetic algorithm," *IEEE Trans. Signal Proces.*, vol. 42, no. 4, pp. 927-935, Apr. 1994.
- [34] J. P. Tang, G. D. He, X. Fu, and Q. Li, "Study on the relevance between the physico-mechanical parameters of foundation soft clay of Foshan," *Chinese J. Underground Space Eng.*, vol. 14, pp. 645-659, Dec. 2018.
- [35] M. H. Zhao, Y. Xiao, and C. F. Chen, "Laboratory experiment of the rheological property of soft clay and the improved Xiyuan model," *J. Hunan Univ.*, vol. 31, no. 1, pp. 48-51, Feb. 2004. DOI: 10.3321/j.issn:1000-2472.2004.01.013.
- [36] C. Y. Zhou, C. M. Mu, "Distribution and microstructure classification of soft clay in the Pearl River Delta," *Acta Sic. Nat. Univ. Sunyatseni*, vol. 43, no. 6, pp. 81-84, Nov. 2004.
- [37] Z. W. Li, X. L. Ding, C. Huang, J. J. Zhu, and Y. L. Chen, "Improved filtering parameter determination for the Goldstein radar interferogram filter," *ISPRS J. Photogramm. Remote Sens.*, vol. 63, no. 6, pp. 621-634, Nov. 2008.
- [38] X. Xing, D. Wen, H. C. Chang, F. C. Li, and H. Y. Zhi, "Highway Deformation Monitoring Based on an Integrated CRInSAR Algorithm—Simulation and Real Data Validation," *Int. J. Pattern. Recognit. Artif. Intell.*, vol. 32, no. 8, 2018.
- [39] A. Hooper, D. Bekaert, K. Spaans, and M. Arıkan, "Recent advances in SAR interferometry time series analysis for measuring crustal deformation," *Tectonophysics*, vol. 514, pp. 1-13, Jan. 2012.
- [40] D. Massonnet, and H. Vadon, "ERS-1 internal clock drift measured by interferometry," *IEEE Trans. Geosci. Remote Sens.*, vol. 33, no. 2, pp. 401-408, March. 1995.
- [41] Z. F. Yang, B. Xu, Z. W. Li, L. X. Wu, and J. J. Zhu, "Prediction of Mining-induced Kinematic 3-D Displacement from InSAR Using a Weibull Model and a Kalman Filter," *IEEE Trans. Geosci. Remote Sens.*, vol. 60, Feb. 2021.
- [42] L. Y. Wang, K. Z. Deng, and M. N. Zheng, "Research on Ground Deformation Monitoring Method in Mining Areas Using the Probability Integral Model Fusion D-InSAR, Sub-band InSAR and Offset Tracking," *Int. J. Appl. Earth Obs.*, vol. 85, no. 101981, Mar. 2020.
- [43] S. S. Shi, "Shear strength, modulus of rigidity and young's modulus of concrete," (in Chinese), *Chin. Civil Eng. J.*, vol. 32, no. 2, pp. 47-52, Apr. 1999.
- [44] F. He, C. E. Woods, J. R. Litowski, L. A. Roschen, H. S. Gadgil, V. I. Razinkov, and B. A. Kerwin, "Effect of Sugar Molecules on the Viscosity of High Concentration Monoclonal Antibody Solutions," *Pharm. Res.*, vol. 28, no. 7, pp. 1552-1560, May. 2011.
- [45] P. Castellazzi, J. Garfias, R. Martel, C. Brouard, and A. Rivera, "InSAR to support sustainable urbanization over compacting aquifers: The case of Toluca Valley, Mexico," *Int. J. Appl. Earth Obs. Geoinf.*, vol. 63, pp. 33-44, Dec. 2017.
- [46] B. Chen, H. Gong, X. Li, K. Lei, L. Zhu, M. Gao, and C. Zhou, "Characterization and causes of land subsidence in Beijing, China," *Int. J. Remote Sens.*, vol. 38, no. 3, pp. 808-826, Dec. 2016.
- [47] F. Cigna, B. Osmanoglu, E. Cabral-Cano, T. H. Dixon, J. A. Ávila-Olivera, V. H. Garduño-Monroy, C. DeMets, and S. Wdowinski, "Monitoring land subsidence and its induced geological hazard with Synthetic Aperture Radar Interferometry: A case study in Morelia, Mexico," *Remote Sens. Environ.*, vol. 117, pp. 146-161, Feb. 2012.
- [48] D. Notti, R. M. Mateos, O. Monserrat, N. Devanthéry, T. Peinado, F. J. Roldán, F. Fernández-Chacón, J. P. Galve, F. Lamas, and J. M. Azañón, "Lithological control of land subsidence induced by groundwater withdrawal in new urban areas (Granada Basin, SE Spain). Multiband DInSAR monitoring," *Hydrolog. Process.*, vol. 30, no. 13, pp. 2317-2331, Jan. 2016.
- [49] J. W. Bell, F. Amelung, A. Ferretti, M. Bianchi, and F. Novali, "Permanent scatterer InSAR reveals seasonal and long-term aquifer-system response to groundwater pumping and artificial recharge," *Water Resour. Res.*, vol. 44, no. 2, Feb. 2008.



Xuemin Xing was born in Liaoning, China, in 1983. She received the B.S. and M.S. degrees and the Ph.D. degree in geomatics and surveying from Central South University, Changsha, China, in 2005, 2008, and 2011, respectively.

From 2016 to 2017, she was a Visiting Scholar with the Department of Environmental Sciences, Macquarie University, Sydney, NSW, Australia. She is currently an Associate Professor with the School of Traffic and Transportation Engineering, Changsha University of Science and Technology, Changsha, where she is also a Key Member of the Laboratory of Radar Remote Sensing Applications. She is also a reviewer for three international journals and four national journals in China. She has authored more than 50 articles and 8 inventions. Her research interest includes the application of time series interferometric synthetic aperture radar (InSAR) technique in highway deformation monitoring, deriving spatial-temporal large-scale deformation induced by mining activities and modeling, and the integration of persistent scatterer (PS), corner reflector (CR), and small baseline subset (SBAS) technique.



Yikai Zhu was born in Hunan, China, in 1997. He received the B.S. degree in geomatics and surveying from Changsha University of Science and Technology, Changsha, China, in 2018 and obtained the M.S. degree in 2021. He is currently a Ph.D. candidate with the Chinese Antarctic Center of Surveying and Mapping, Wuhan University.

His research interests focus on the application of time series interferometric synthetic aperture radar (InSAR) technique to study large traffic infrastructures deformation, ground-based InSAR (GB-InSAR), polar remote sensing, and global environmental change.



Wenbin Xu received the Ph.D. degree in geophysics from the King Abdullah University of Science and Technology (KAUST), Saudi Arabia, in 2015.

He leads the Lab of Volcano and Earthquake Research and is a Full Professor with the Department of Surveying and Remote Sensing, School of Geosciences and Info-Physics, Central South University. His research focuses on the use of satellite remote sensing and radar interferometry (InSAR) to study crustal deformation due to a variety of geophysical and anthropogenic processes, such as earthquake cycle, volcanic activity, and ground water withdrawal.



Wei Peng received the PhD degree in geodesy from Central South University, China, in 2020, and during Oct. 2017 to Oct. 2018, he was sponsored by the China Scholarship Council (CSC) to study at Texas State University-San Marcos, Texas, USA, as a joint PhD student in geography.

He is currently a lecturer at Changsha University of Science & Technology, China. His research interests are GPS and InSAR data processing, non-tectonic deformation.



Zhihui Yuan was born in Hunan, China, in 1983. He received the B.S. degree in electronic information engineering from Xiangtan University, Xiangtan, China, in 2007, and the Ph.D. degree in communication and information systems from the Institute of Electronics, Chinese Academy of Sciences, Beijing, China, in 2013.

Since 2013, he has been a Lecturer with the School of Electrical and Information Engineering, Changsha University of Science and Technology, Changsha, China. From 2018 to 2019, he was a Visiting Scholar with the Roy M. Huffington Department of Earth Sciences, Southern Methodist University, Dallas, TX, USA, working with Prof. Z. Lu on the interferometric synthetic aperture radar (InSAR) technique. He is also a Principal Investigator of the scientific project Research on Multichannel InSAR Robust DEM Inversion with High Precision for Complicated Terrain supported by the National Natural Science Foundation of China. His research interests include signal processing and the application of synthetic aperture radar interferometry, phase unwrapping, high-resolution digital elevation model generation, and algorithm design.